



HAL
open science

Mechanisms of aromatization of dilute ethylene on HZSM-5 and on Zn/HZSM-5 catalysts

Aurélien Bonnin, Jean-Dominique Comparot, Yannick Pouilloux, Vincent
Coupard, Denis Uzio, Ludovic Pinard

► **To cite this version:**

Aurélien Bonnin, Jean-Dominique Comparot, Yannick Pouilloux, Vincent Coupard, Denis Uzio, et al..
Mechanisms of aromatization of dilute ethylene on HZSM-5 and on Zn/HZSM-5 catalysts. Applied
Catalysis A : General, 2021, 611, pp.117974. 10.1016/j.apcata.2020.117974 . hal-03159920

HAL Id: hal-03159920

<https://ifp.hal.science/hal-03159920>

Submitted on 3 Feb 2023

HAL is a multi-disciplinary open access archive for the deposit and dissemination of scientific research documents, whether they are published or not. The documents may come from teaching and research institutions in France or abroad, or from public or private research centers.

L'archive ouverte pluridisciplinaire **HAL**, est destinée au dépôt et à la diffusion de documents scientifiques de niveau recherche, publiés ou non, émanant des établissements d'enseignement et de recherche français ou étrangers, des laboratoires publics ou privés.



Distributed under a Creative Commons Attribution - NonCommercial 4.0 International License

Mechanisms of aromatization of dilute ethylene on HZSM-5 and on Zn/HZSM-5 catalysts

Aurélien Bonnin¹, Jean-Dominique Comparot¹, Yannick Pouilloux¹, Vincent Coupard²,
Denis Uzio², Ludovic Pinard*¹

¹Institut de Chimie des Milieux et Matériaux de Poitiers (ICM2P), UMR 7285 CNRS, 4 Rue Michel Brunet, Bâtiment B27, 86073 Poitiers Cedex – France.

²IFP Energies nouvelles, Etablissement de Lyon, Rond-point de l'échangeur de Solaize - BP 3, 69360 Solaize – France

*Corresponding author ludovic.pinard@univ-poitiers.fr

Abstract

Catalysts with a Zn/H⁺ molar ratio ranging from 0 (H-ZSM5) to 1.8 (Zn/H-ZSM5), were prepared by wet impregnation from three commercial zeolites with Si/Al ratio of 15, 40 and 75. The texture, acidity and reactivity of the bifunctional catalysts were characterized by: N₂, IR followed by adsorption of pyridine and NH₃-TPD, and tested at 500 °C with low partial pressure of ethylene (P_{C₂H₄} = 0.005 MPa) and a high GHSV (ca 13300 h⁻¹).

The intrinsic activity of protonic acid sites in ethylene transformation depends on their density or rather on the concentration of next nearest neighbours pairs of Al atoms. Brønsted acid pair sites converts ethylene into aromatics while isolated protonic site are almost inactive. Two apparent primary products were distinguished: iso-butene and propene, resulting from the oligomerization-cracking catalytic pool, followed at high conversion by the concomitant formation of alkanes and aromatics through hydrogen transfer.

The deposition of Zn was achieved by wet impregnation of the nitrate precursor. The thermal decomposition of the ZnOH⁺ cation by calcination is a function of the fraction of Al atoms in the nearest neighbours. Three main species of Zn could be identified: i) oxo-binuclear Zn²⁺ cations (O⁻-Zn²⁺-O-Zn²⁺-O⁻), ii) mononuclear Zn²⁺ cations (O⁻-Zn²⁺-O⁻ and iii) ZnO particles located on the external surface. These species were quantified from the residual Brønsted acid sites probed by pyridine. A correlation has been established: one neutralized protonic site generates one Zn Lewis acid sites which coordinates two pyridine molecules. The ethylene conversion is proportional to the concentration of oxo-binuclear Zn cations and mononuclear Zn cations only correlate with hydrogenation and hydrogenolysis of olefins, while bulk ZnO is inactive.

A metallacyclic mechanism of ethylene aromatization involving cyclo-butyl-zinc species has been proposed accordingly.

Key words: Zn/H-ZSM-5, dilute ethylene, reaction mechanisms, aromatization, active sites.

40

41 **Introduction**

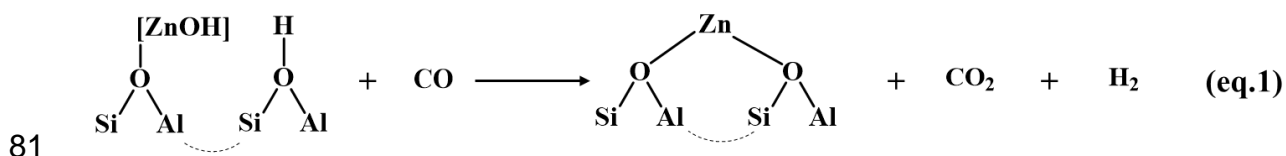
42 Pervasive in our daily lives as plastics, packaging, clothing, digital devices, medical
43 equipment, tyres etc., petrochemicals provide substantial benefits to society, including a
44 growing number of applications in various cutting-edge, clean technologies critical for
45 sustainable energy economy. They are set to account for more than a third of the growth in oil
46 demand to 2030, and nearly half in 2050. [1] Meanwhile, oil demand for the production of
47 transportation fuel is expected to decrease due to the combined effects of improved fuel
48 economy, alternatives fuels and electrification. As a result, the landscape for the
49 petrochemical, oil and gas industries is shifting toward “High-Value Chemicals” (HVCs) such
50 as light olefins (ethylene and propylene) and aromatics (benzene, toluene and mixed xylenes,
51 (BTX) which are the building blocks for many value-added chains.

52 Some “by-products” from oil refining are now considered more like “co-products” or
53 even “primary products”. For instance, the FCC dry gas containing ethylene (5 to 50% by
54 weight) and ethane is currently used as refinery fuel. [2] Since 50,000 barrels per day for a
55 FCC unit burn approximately 200 tons of dry gas per day, 10-100 tons of ethylene are burned
56 each day. A diligent option would be to transform ethylene into value-added products such as
57 propylene or aromatics. Over the past decade, several companies developed technologies for
58 the oligomerization and aromatization of concentrated ethylene from dry gas: $3 \text{C}_2\text{H}_4 \rightarrow \text{C}_6\text{H}_6$
59 $+ 3\text{H}_2$. The Beijing Huiersanji Green Chem DTL process licensed by Invista Performance
60 Technologies is the most mature, with 12 operating units in China in 2018. [3] Wood and
61 Siluria Technologies launched Modus TM, the first treatment technology to convert FCC gases
62 into refinery products, and UOP LLC developed a process that converts more than 40% of
63 ethylene into fuels in a single pass.

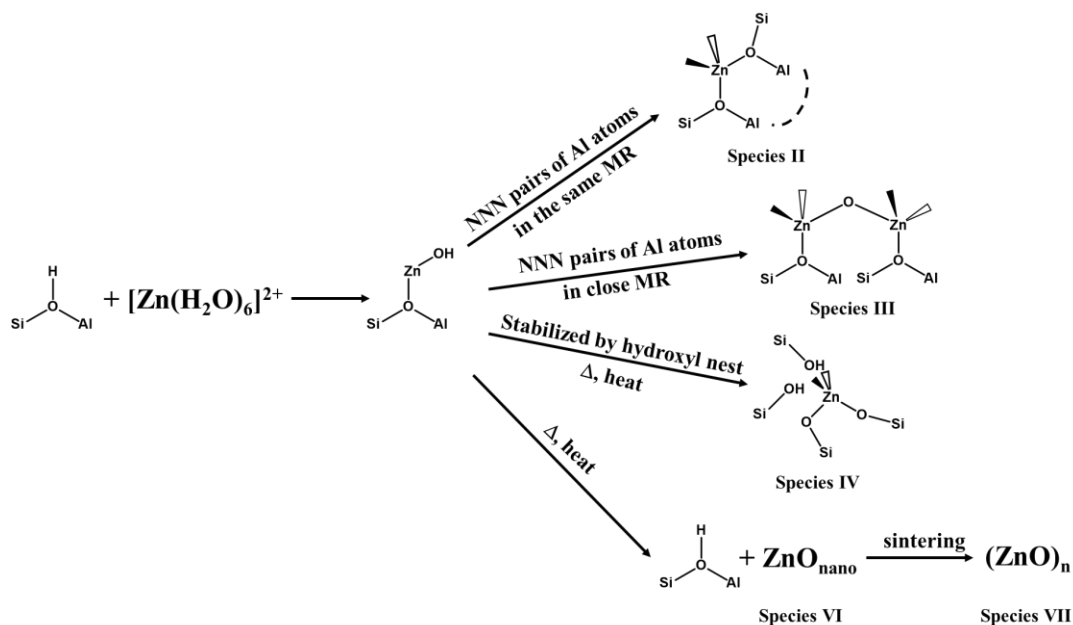
64 Zn-loaded H-ZSM-5 is a promising catalyst for the aromatization of ethylene due to
65 the specific dehydrogenation/hydrogenation performances of the metal cation [4-6] and the

66 high selectivity towards aromatics related to the size and shape of the zeolite micropores.
 67 However, the role of Zn metallic site is still unclear. The oxidation states of Zn species are
 68 limited to 0, +1 and +2. Considering that the total reduction of (ZnO)_n is hardly achieved even
 69 by hydrogen treatment at 600 °C [7] and Zn (+1) has never been observed in zeolites, the
 70 formal oxidation state of Zn in zeolite is expected to be +2.

71 Ion exchange and wetness impregnation are typical preparation methods. The hexaaquo Zn
 72 complex ion acts as an acid by giving a hydrogen ion to water molecule in the aqueous
 73 solution ($[Zn(H_2O)_6]^{2+} + H_2O \rightleftharpoons [ZnOH(H_2O)_5]^+ + H_3O^+$). The monovalent cation can be
 74 exchanged with all the zeolite protons. Water from the aqua complex is stepwise removed
 75 during calcination resulting in the formation of [ZnOH]O_z species (**species I**) [8], which was
 76 described as the active site for the formation of aromatics from ethylene [9], *n*-pentane [10],
 77 and methanol [11-13]. Bernt et al. identified this species using a temperature-programmed
 78 surface reaction with CO (TPSR / CO). [14] Since the CO reaction on protonic ZSM-5
 79 (Si/Al=23) zeolite gives equimolar amounts of CO₂ and H₂, the authors proposed the
 80 following reaction equation:



82 CO inserts in the OH group of Zn species, giving a formate species that reacts with a
 83 neighbouring H⁺ and decomposes into CO₂ and H₂. Yet, Biscardi et al. showed by X-ray
 84 adsorption experiments that the [ZnOH]O_z species was not thermally stable. [15] Their
 85 decomposition paths depends on the Al atom fraction in the next nearest neighbours (NNN)
 86 position (**Scheme 1**).



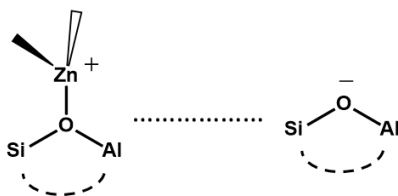
87

88 **Scheme 1:** Different possible species of Zn cations on zeolite H-ZSM-5 after ion exchange
 89 and wet impregnation followed by calcination.

90 Rice et al. [16] calculated by stochastic simulations the probability in ZSM-5 zeolite of NNN
 91 pairs of Al atoms able to stabilize a divalent cation (M^{2+} , **Species II**) and form an oxo-
 92 binuclear cation, i.e. two M^{2+} bridged by an oxygen atom ($-M-O-M-)^{2+}$ (**Species III**). The
 93 assessment of the maximum probability to form bridged M^{2+} cations is 0.12 for Si/Al =12 and
 94 decreases to 0.07 with half of the framework aluminium (Si/Al =24) (**Figure SI.1**). Relative
 95 to the binuclear oxo metal cation, the probabilities are higher: 0.30 and 0.19 for Si/Al =12 and
 96 24, respectively. The distribution of the Zn cation species therefore depends on the zeolite
 97 Si/Al ratio (**Figure SI.1**). It is worth mentioning that the divalent cation can also be stabilized
 98 by being linked by an Al centred tetrahedron and an internal silanol group in its vicinity
 99 (**Species IV**). [17]

100 In the case of the catalyst prepared through ion exchange or wetness impregnation, the
 101 exchange is commonly 60%. [18] Thus, the isolated cationic $(ZnOH)^+$ species cannot be
 102 stabilized during calcination and decomposes into ZnO nanoclusters (**Species VI**)
 103 regenerating the initial Brønsted acid site.

104 Complete substitution of framework aluminium is only possible through the chemical
105 deposition method [17,19]. This preparation method also allows an unusual location of Zn^{2+}
106 cations [18,20], which is stabilized at an ionic site of the zeolite with a distantly located
107 second charge-compensating (AlO_2^-) framework unit (**Species V, Scheme 2**).



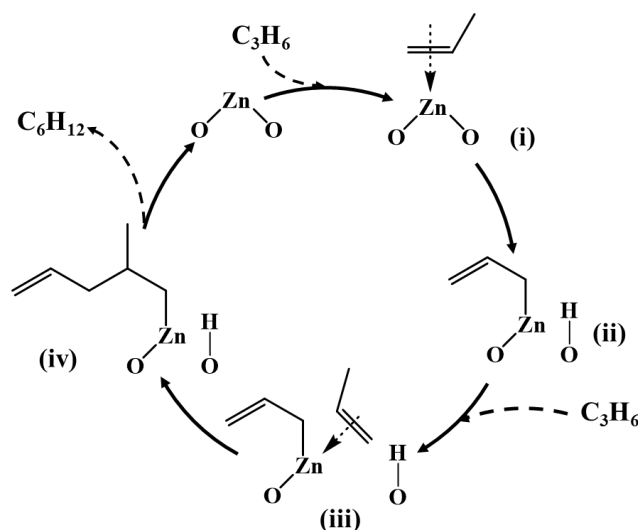
108
109 **Scheme 2:** Zn cation species (Species V) with alternating positive and negative electric
110 charges.

111 Hence, Zn/H-ZSM-5 catalyst prepared using conventional techniques leads to
112 $(ZnOH)^+$ which decomposes into a bridging Zn^{2+} cation by two framework aluminium
113 (**Species II**), or by a framework aluminium (FAL) and an internal silanol (**Species IV**), a
114 binuclear oxo Zn cation (**Species III**), and nanoclusters of zinc oxide (**Species IV**).

115 UV-Vis diffuse reflectance spectroscopy can distinguish subnanometric ZnO clusters
116 within the zeolite micropores (275 nm, [21-22]) from large $(ZnO)_n$ particles on the external
117 surface (375 nm, [23-24] **Species VII**). Temperature programmed reduction allows the
118 detection of zinc oxide, since its reduction starts around 580 °C. In contrast, Zn^{2+} is stable
119 even at 880 °C. [15] Large $(ZnO)_n$ crystals can be considered as spectator species, due to their
120 inactivity in the aromatization of ethane [25], propane [15] and CO activation [14].
121 Nanocrystals $(ZnO)_n$ catalyse dehydrogenation reaction but impede the diffusion of products,
122 thus deteriorating the stability of the catalyst. [11]

123 Zn cation species are involved in the dehydrogenation step but mainly catalyze the
124 recombination-desorption of H atoms into H_2 , which is considered to be the rate limiting step
125 in alkane aromatization. [26-28] The mechanism here is bifunctional because the Brønsted
126 acid sites allows the di/trimerization of the olefins, which are then cyclized: $2 C_3H_8$

127 $\xrightarrow{Zn} 2 C_3H_6 + 2H_2 \xrightarrow{H^+} C_6H_{12} \xrightarrow{Zn} C_6H_6 + 3H_2$. This bifunctional mechanism of olefins to
 128 aromatics is commonly accepted by the scientific community. [29] However, Lobo et al
 129 suggested that Zn in the form of Lewis acid sites can lead to the oligomerization of ethylene.
 130 [25] Indeed, Stepanov et al. [30-31] have shown by ^{13}C MAS NMR and FTIR spectroscopic
 131 studies that Zn cation species on ZSM-5 zeolite oligomerize propylene. The stages of the
 132 proposed mechanism follow a Cosse-Arlman mechanism and can be summarized as follows
 133 **(Scheme 3)**: i) propylene adsorption on a Zn^{2+} site ii) dissociation of propylene resulting in a σ
 134 allylzinc species and a Si-O(H)-Al group, iii) adsorption of a second propylene molecule on
 135 the Zn sites forming a new π -complex, iv) recombination of the π -complex and of the
 136 allylzinc species, and v) desorption of C_6H_{12} and regeneration of active site.



137
 138 **Scheme 3:** Mechanism of propylene oligomerization on Zn^{2+}/H -ZSM-5 cation, adapted from
 139 [30].
 140

141 Hence, the possibility that oligomerization of olefins may occur on Zn cation species
 142 raises the question of the bifunctional mechanism of ethylene aromatization on Zn/ZSM-5
 143 zeolite. The goal of this study is to identify the mechanisms and the active sites of the
 144 ethylene aromatization over H-ZSM-5 and Zn/H- ZSM-5 catalysts. We will demonstrate that

145 the intrinsic activity of the protonic acid sites depends on the concentration of the next nearest
146 neighbours Al atom pairs and that on the bifunctional catalyst, ethylene aromatization occurs
147 by monofunctional catalysis via a metallacyclic mechanism on oxo-binuclear Zn^{2+} cations.
148 For this purpose, more than 15 catalysts with a molar balance between the two functions
149 (Zn/Al) ranging from 0 (H-ZSM5) to 1.8 (Zn/H-ZSM5), were prepared, characterised by
150 different probe molecules (N_2 , pyridine and NH_3), and tested with dilute ethylene at 500 °C.
151 This paper focuses only on the initial conversion and does not take into account the
152 deactivation that occurs during the ethylene aromatization, this point is discussed in another
153 publication.

154 **Experimental**

155 **Materials:** Three series of Zn-containing catalysts were prepared from three commercial
156 zeolites (Zeolyst) with global Si/Al molar ratios of 15 (CBV 3042E), 40 (CBV 8014) and 75
157 (CBV 1502) zeolites. The CBV 3042E and CBV 8014 under ammonium form were calcined
158 in air at 500 °C. Another commercial protonic zeolite with a Si/Al molar ratio of 25 (CBV
159 5020) was also used.

160 Zn-containing zeolites were prepared by wet impregnation by stirring protonic zeolite
161 with an aqueous solution of $Zn(NO_3)_2 \cdot 6H_2O$ at 60 °C for 30 minutes, in the proportion of 1 g
162 of zeolite per 10 mL of solution. Then, the samples were dried at 120 °C for 12 h and calcined
163 at 500 °C under air (60 mL min^{-1}) for 12 h.

164 $0.8Zn40^{IE}$ was prepared by ion exchange by stirring HZ40 under ammonium form in an
165 aqueous solution of $Zn(NO_3)_2 \cdot 6H_2O$ ($m/V = 0.02 \text{ g l}^{-1}$) at 80 °C for 2h. In contrast to wet
166 impregnation, the sample is rinsed with water. Ion exchange was carried out successively
167 three times before drying and calcination. $0.8Zn40^{DI}$ was prepared by dry impregnation, with
168 a volume of the metal solution equivalent to the micropore volume of the zeolite i.e. 0.18 cm^3

169 $\text{g}^{-1}_{\text{zeolite}}$. All zeolites under protonic form and bifunctional catalysts are calcined at 500 °C
170 before catalytic test.

171 **Characterizations:** The elemental composition of the bifunctional catalysts (Si, Al,
172 Zn) was determined using an inductively coupled plasma-atomic emission spectroscopy (ICP-
173 AES) on an Optima 2000 DV (Perkin-Elmer). The samples (30-40 mg) were mineralized by
174 three successive acid attacks by HNO_3 (69 vol. %), HCl (37 vol. %) and HF (40 vol. %) in the
175 proportion of 4/2/2 mL, respectively. Mineralization was carried out in sealed vessels at 180
176 °C under an autogenous pressure of 2.0 MPa for 45 min using a microwave oven (Anton-Parr
177 Multiwave Pro). Finally, 12 mL of a saturated solution of H_3BO_4 was added to the sample.

178 Samples were characterized by transmission electronic microscopy (TEM) using a
179 JEOL 2100 microscope equipped with a LaB_6 filament operating at 200 kV. The samples
180 were first prepared by ultrasonic dispersion in ethanol and then dropped onto a copper grid,
181 previously covered with a carbon film.

182 Nitrogen adsorption and desorption measurements were carried out at -196 °C on a
183 Micromeritics ASAP 2420 apparatus. Before analysis, the samples were pre-treated at 350 °C
184 under vacuum for 15h. The micropore volumes (V_{micro}) were calculated according to the t -plot
185 method and the total pore volume was calculated at $p/p_0 = 0.98$.

186 ^{27}Al magic angle spinning nuclear magnetic resonance (^{27}Al MAS NMR) spectra were
187 recorded at 104.28 MHz on a Bruker advance II 400 MHz spectrometer using a spinning rate
188 of 12 kHz, a pulse length of 0.42 μs and a recycle time of 0.5 s.

189 The nature, concentration of acidity were studied using adsorption of pyridine
190 followed by infrared spectroscopy (FTIR) with a Nicolet 5700 apparatus with 2 cm^{-1} optical
191 resolution. Prior to analysis, the catalyst was pressed (0.5 ton) into a self-supporting wafer (2
192 cm^2) and pretreated from 20 °C to 500 °C under nitrogen flow ($100\text{ cm}^3\text{min}^{-1}$). The sample
193 was then degassed (10^{-5} bar) during 1h at 200 °C, after which an IR spectrum was taken. The

194 sample was then cooled to 150 °C and exposed to a pyridine pressure of 1.5 mbar for 5 min
195 and then degassed (10^{-5} bar) to remove the physisorbed pyridine. The Beer-Lambert-Bouguer
196 law was applied in the form $[PyH^+] \text{ or } [PyL] = \left(\frac{S}{m}\right) \frac{A}{\epsilon}$ where $[PyH^+]$ and $[PyL]$ is the
197 concentration of Brønsted and Lewis acid sites ($\mu\text{mol g}^{-1}$), A denotes the integrated
198 absorbance of the corresponding IR bands (1545 and 1455 cm^{-1}), which is normalized to
199 zeolite wafer density (ratio of the wafer weight (mg) to wafer surface (cm^2), and ϵ is the
200 integrated molar adsorption coefficient: $\epsilon_{1545} = 1.13$ and $\epsilon_{1454} = 1.28 \text{ cm mol}^{-1}$. [32] The
201 calibration curves were obtained on a MFI (Si/Al=27) and a $\gamma\text{-Al}_2\text{O}_3$ by adding to the IR cell
202 a known amount of pyridine vapour from gas inlet compartment (0.9122 cm^3) (**Figure. SI.2**).
203 All the reported FTIR spectra are normalized to a wafer density (mg cm^{-2}).

204 The temperature-programmed desorption of ammonia (NH_3 -TPD) profiles were
205 measured using a flow-through micro-reactor system connected to a thermal conductivity
206 detector (TCD). The samples (0.4 g) were activated under helium at 500 °C for 1 hour then
207 cooled to 100 °C, prior to adsorption of ammonia (5 vol. % in He) for 45 minutes. The
208 physisorbed ammonia was removed by purging with helium at 100 °C for 3 hours. Ammonia
209 desorption was achieved in the temperature range of 100 to 550°C with a heating rate of 5 °C
210 min^{-1} under He.

211 **Catalytic test:** A typical catalytic test for the ethylene conversion (Air Liquid, > 99%)
212 was carried out at atmospheric pressure in a fixed-bed continuous flow quartz reactor at 500
213 °C with a N_2 /reactant molar ratio of 19, which correspond to an ethylene partial pressure of
214 0.005 MPa. Under standard conditions, the weight gas hourly space velocity WHSV (g of
215 injected C_2H_4 per hour and per g of catalyst) was 2 h^{-1} , and the gas hourly space velocity was
216 $13\,300 \text{ h}^{-1}$ which corresponds to a short contact time of $7.5 \times 10^{-5} \text{ h}$. For the kinetic study, the
217 GHSV varied from 13 300 to 213 400 h^{-1} . Prior to testing, catalysts were compacted, crushed
218 and sieved to obtain homogeneous particles (0.2-0.4 mm). Samples were pre-treated at 500 °C

219 under nitrogen flow (100 mL min^{-1}) for 1 h. The gaseous products and hydrogen were
220 analysed on-line by a Varian CP-3800 gas chromatograph equipped with a FID detector
221 connected to a fused silica J&W GS-Gaspro capillary column ($60 \text{ m} \times 0.32 \text{ mm} \times 4 \text{ }\mu\text{m}$) and
222 a TCD connected to a J&W PoraPLOT Q-HT capillary column ($25 \text{ m} \times 0.53 \text{ mm} \times 20 \text{ }\mu\text{m}$).

223 The catalytic results in this study relate only to the conversions and yields measured
224 after 10 minutes of reaction.

225 **Results and discussion**

226 **1. Textural and acidic properties of the four commercial H-ZSM-5 zeolites.**

227 The protonic zeolites are named HZ followed by their Si/Al molar ratio. The textural
228 properties of commercial zeolites are given in the supporting information (**Table SI.1**).
229 Microporous volumes between $0.15\text{-}0.18 \text{ cm}^3 \text{ g}^{-1}$ were inferred for these samples, which is a
230 typical value for ZSM-5 zeolites. [33] In addition, mesopore volumes between $0.11\text{-}0.14 \text{ cm}^3$
231 g^{-1} were deduced. Mesopores on HZ15 result from the aggregation of the small crystals as
232 indicated by the strong nitrogen uptake at high relative pressure (**Figure. SI.3 and Figure**
233 **SI.4**), while on HZ40 and HZ75 the mesopore volume is rather intraparticular (**Figure SI.4**)
234 as shown by the presence of a hysteresis loop of type IV (**Figure SI.3**). The intraparticular
235 mesopores are probably generated during the steaming process applied during the preparation
236 of the sample by the supplier.

237 **Figure 1a** compares the infrared spectra in the OH stretching region of the three zeolites.
238 HZ75 has two IR bands: an intense band at $3610 \text{ cm}^{-1} (\pm 2)$ attributed to the bridged hydroxyl
239 groups (Si-O(H)-Al) and an asymmetric band at 3740 cm^{-1} ascribed to the terminal silanol
240 groups on the external surface. On HZ40, the shoulder at 3726 cm^{-1} corresponds to Si-OH
241 located on the intraparticular defects and is correlated with the broad band centred at 3470 cm^{-1}
242 1 , which is assigned to the hydroxyl nests. These internal defects are microcavities saturated
243 with neighbouring OH groups close enough to interact through hydrogen bonds. [34] ^{27}Al

244 MAS NMR on HZ40, confirms that almost all of the Al ($\geq 95\%$) are of tetrahedral
245 coordinated and thus within the zeolite framework (**Figure SI.5**).

246 HZ25 and HZ15 exhibit an intense band at 3665 cm^{-1} which corresponds to OH linked to
247 extraframework aluminium species (e.g. AlOH^+). Chemisorption of pyridine at $150\text{ }^\circ\text{C}$ leads
248 to a total disappearance of the bridged hydroxyl groups on the four zeolites, while the
249 intensity of the silanol bands remains unchanged. The concentrations of the Brønsted acid
250 sites able to retain pyridine at this temperature on H-ZSM-5 zeolites with Si/Al of 15, 25, 40,
251 and 75 are of 515, 307, 286, and $148\text{ }\mu\text{mol g}^{-1}$, respectively (**Table 1**). The number of
252 bridging acid sites in typical commercial MFI zeolites is significantly lower with respect to
253 their Al content (i.e. 1041, 640, 386 and $219\text{ }\mu\text{mol g}^{-1}$, respectively). However, the
254 quantification of the BAS is in agreement with these of White et al. obtained from ^1H MAS
255 NMR spin counting (4.2 ppm peak). [35] For instance, on Si/Al = 15 they found a
256 concentration of BAS of $560 \pm 18\text{ }\mu\text{mol g}^{-1}$, which is about the same as that measured by
257 pyridine adsorption followed by FTIR, i.e. $515\text{ }\mu\text{mol g}^{-1}$. This means that 60-70% of the
258 theoretical protons exists as BAS, with the other distributed among the other distorted
259 framework sites or other nonframework sites. [35] Gabrienko et al. also found that on the
260 commercial zeolite with Si/Al of 40 (CBV-8014), the concentration of BAS measured by ^1H
261 MAS NMR is $312 \pm 28\text{ }\mu\text{mol g}^{-1}$, which is close to the concentration measured in this study,
262 i.e. $286\text{ }\mu\text{mol g}^{-1}$. [36]

263 In addition, on HZ15 and HZ25 zeolites, one part of EFAL species chemisorbs pyridine
264 (**Figure SI.6**) resulting in a slight increase in the concentration of Lewis acid sites (ca 15
265 $\mu\text{mol g}^{-1}$). The presence of the iminium ion, indicated by the band centred at 1462 cm^{-1} [37]
266 (**Figure 1b**), suggests a close proximity of the bridged OH groups with the EFAL species
267 (**Figure SI.7**).

268

269 **2. Textural and acidic properties of the three series of bifunctional catalyst: 15, 40**
270 **and 75.**

271 Zn-based catalysts are referred to as $x\text{Zn}_y$ where x is the zinc content and y the Si/Al
272 molar ratio. Three series of bifunctional catalysts were prepared by wetness impregnation
273 from HZ15, HZ40 and HZ75 zeolites with a Zn loading ranging from 0.3 to 8.1 wt. % (**Table**
274 **1**). Zn loading on HZ40 was also prepared by ion exchange and dry impregnation: $0.8\text{Zn40}^{\text{IE}}$
275 and $0.8\text{Zn40}^{\text{DI}}$

276 2.1 Zn40 and 3.6 Zn40 exhibit similar characteristic of MFI structure, as shown in **Fig.**
277 **SI.7**, suggesting that the introduction of Zn species by wet impregnation has no impact in the
278 zeolite framework. Only very weak diffraction peaks of ZnO at 36.3° and 31.8° are observed.

279 **Figure 2** shows the micropore volume (V_{micro}) as a function of the Zn content. For the
280 HZ15 and HZ75 catalyst series, the micropore volume is only slightly affected by the high Zn
281 loading, probably due to the deposition of a small amount of subnanometric $(\text{ZnO})_n$ particles
282 (**Species IV**) in the micropores. On the other hand, for the series HZ40, V_{micro} decreases with
283 increasing Zn content, suggesting that on this zeolite, which has internal defects, the Zn oxide
284 species may be located in the microcavities formed by the hydroxyl nests.

285 The TPR study on 2.1Zn40 shows no reduction. Indeed, Biscardi and al have shown that
286 Zn^{2+} cations in ion-exchanged 1.07Z14.5 do not reduce even at 877°C and ZnO crystals begin
287 to reduce to Zn metal and sublime around 480°C in flowing hydrogen. [15] Moreover, the
288 absence of metal Zn is confirmed by the fact that after 5 hours of reaction, the Zn content
289 remains stable on all catalysts. It should be noted that a pretreatment of 2.1Zn40 under H_2 at
290 500°C has no impact on activity and selectivity, suggesting that the oxidation state of Zn is
291 +2. (**Table SI.1**)

292 The intensities of the bridged OH-band of the three catalysts series (**Figure 3**) decrease
293 partially, even with a Zn content in solution two to three times higher than their exchange

294 capacity, which is calculated assuming a Zn/Al molar ratio of 0.5 (1/2), i.e. 0.7, 1.4 and 3.4
295 wt. % on HZ75, HZ40 and HZ15, respectively (**Table 1**). Therefore, only a limited fraction of
296 the proton can be substituted by Zn^{2+} cations. Most theoretical research has shown that the
297 exchange of the cationic position corresponds to two aluminium atoms in the same four or
298 six-membered ring in which Zn^{2+} coordinates four zeolite oxygens. [38-40] Yet the fraction of
299 aluminum at the sites in the next-nearest position is rather limited. For the high-silica zeolite
300 (HZ75), the consumption of bridged OH groups is limited due to the low probability of
301 finding two Al ions in the same ring. [16] It is worth mentioning that complete substitution of
302 proton by zinc ions even with a high-silica zeolite, can be achieved by chemical reaction with
303 zinc vapour. [18,20]

304 Regardless of the Zn loading mode (wet and dry impregnation, and ion exchange), the IR
305 spectra of OH region are similar. (**Figure SI.8**). For all three zeolites, the consumption of Si-
306 O(H)-Al groups is concomitant with the increase of the band at 3665 cm^{-1} . This latter is not
307 related to EFAL species since the ^{27}Al NMR spectra of 1.8Zn40 and 5.6Zn40 show only one
308 peak centred at 50 ppm characteristic of framework aluminium (**Figure SI.5**). Some authors
309 attribute the band at 3665 cm^{-1} on the Zn based catalyst to the cationic species ZnOH^+
310 (**Species I**) [41], but this latter is not stable and undergoes dehydration during calcination
311 [15]. This band cannot be ascribed to hydroxylated zinc oxide, because the adsorption of
312 hydrogen on $(\text{ZnO})_n$ gives an intense band at 3483 cm^{-1} [42]. The intensity of external silanols
313 remains almost unchanged with the Zn loading, in contrast to those located in silanol nests
314 (3470 cm^{-1}), which disappear completely. This suggests that Zn^{2+} cations are stabilized by
315 their interaction with hydroxyl in silanol nests (**species IV**), which is consistent with the
316 previously observed decrease in micropore volume (**Figure 2**). The incorporation of the metal
317 into the framework of HZ40 is confirmed by UV-vis adsorption spectroscopy (**Figure SI.9**),
318 which shows an adsorption band at about 265 nm. This was attributed by Zhang et al. to Zn in

319 the zeolite framework [43] (**Species IV**). An adsorption band at about 370 nm which
320 corresponds to the band gap width of macrocrystalline ZnO (**Species VII**) [8] appears when
321 the Zn loading exceeds 1.4 wt.%. Incorporation of Zn into the MFI framework can be done
322 by isomorphic substitution by healing silanol nests. [44-45] The formation of **species IV** is
323 directly related to the presence of internal defects in the zeolite crystal, therefore the
324 incorporation of Zn into the zeolite framework is only possible in the 40 series.

325

326 TEM images (**Figure SI.10**) clearly show that some $(\text{ZnO})_n$ particles cover the external
327 surface of the HZ40 zeolite. On the 3.6Zn40 catalyst, their size (9.1 nm, **Table 1**) is twelve
328 times larger than the diameter of the larger void volume within the MFI framework, i.e. 0.70
329 nm in the channel intersections. [32] It appears that Zn cations, which do not exchange with
330 zeolite protons, precipitates as $(\text{ZnO})_n$ species and grow on the outer surface during the
331 solvent evaporation step. Their size therefore depends in part on the exchange capacity of the
332 zeolite. The $(\text{ZnO})_n$ particles in 4.1Zn15 and 2.7Zn75 (**Table 1**) were measured 6.8 and 14.8
333 nm, respectively.

334 **Figure 4** shows the NH_3 -TPD profiles obtained for all catalyst series. It should be
335 noted that the shape and location of the peaks depend on the experimental conditions, i.e.,
336 heating rate or gas flow rate, making this technique rather inadequate for quantifying acid
337 sites [46] However, under identical experimental conditions, the position of the peak provides
338 information on the relative acid strength and the width of the peak on the strength distribution.
339 The NH_3 -TPD profiles of acidic ZSM-5 zeolite exhibit two distinct peaks at low (L.T.P.) and
340 high temperatures (H.T.P.), ca $215\text{ }^\circ\text{C} \pm 15$ and $460\text{ }^\circ\text{C} \pm 25$, respectively. The higher the
341 Si/Al ratio, the higher the desorption temperature and the higher the intensity ratio between
342 the high and low temperature peaks. The strength of the acid sites is higher on HZ15 due to
343 the presence of EFAL species. Regardless of the Si/Al ratio, the L.T.P intensities remain

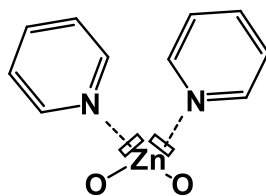
344 almost constant after Zn impregnation. On the other hand, H.T.P. decreases partially on
345 HZ75, even with a high Zn loading, which excludes pore-blocking by ZnO species. [12] On
346 HZ15 and HZ40 zeolites, the high temperature peaks disappear completely after addition of a
347 low Zn content. The disappearance of HTP is concomitant with the appearance at ca 280 °C
348 of shoulders to low temperature peak. Niu et al. attributed the shoulder peak to the medium
349 acid sites of Lewis type derived from the zinc species. [13]

350 Pyridine adsorbed on zeolites leads to characteristic bands at 1546 and 1454 cm^{-1}
351 which reflect pyridine protonated at Brønsted acid (BAS) and ring stretching vibration of
352 pyridine coordinated to Lewis acid (LAS) sites, respectively. The intensity of these two bands
353 decreases and increases concomitantly with Zn impregnation (**Table 1, Figure SI.11**). This
354 indicates a neutralization of the protonic sites by the creation of Zn Lewis acid sites and that
355 pyridine adsorbs in a similar way on Zn^{2+} as on Al^{3+} Lewis acid sites. [47] The concentration
356 of pyridinium ions neutralized increases initially with the addition of Zn and then very
357 slightly incorporation of additional metals (**Figure 5a**).

358 The disappearance of the bridging OH groups (Si-O(H)-Al) remains partial,
359 (comprised, between 40 to 70%), despite impregnation of a Zn content much higher than that
360 required for exchange capacity (**Table 1, Figure 3**). The decrease of the intensity of the
361 bridging OH band is proportional to the decrease of the concentration of Brønsted acid sites
362 (**Figure SI.12**). Therefore, we can evaluate the integrated molar adsorption coefficient ϵ_{OH} for
363 IR band of the bridged Si-O(H)-Al through the ratio of the integrated intensity of this band to
364 the concentration of BAS measured by pyridine. ϵ_{OH} for the band at 3610 cm^{-1} is 2.7 cm
365 μmol^{-1} , which is close to that determined by Gabrienko (3.06 $\text{cm} \mu\text{mol}^{-1}$). [36]

366 The exchange capacity of zeolites with respect to a divalent cation depend not only on
367 the concentration of aluminium in the zeolite framework, but also on their distribution, i.e. the
368 fraction of Al in next nearest neighbours. In other words, during calcination, the NNN Al

369 exchange sites convert $[\text{ZnOH}]\text{O}_z$ (**Species I**) to Lewis acid sites (**Species II and/or III**
 370 **and/or IV**), while isolated Al exchange sites yield $(\text{ZnO})_n$ (**Species V and VII**) which thus
 371 regenerates the Brønsted acid sites. The concentration of the Zn-based Lewis acid sites
 372 follows the same trend as the neutralization of the Brønsted acid sites (**Figure 5b**). The ratio
 373 between the neutralized BAS and created LAS is two, regardless of the mode of Zn loading
 374 (**Figure 5c**). Moreover, this is consistent with the results obtained on Zn-based catalysts
 375 prepared by ion exchange (**Figure 5c**, [9]). Yet, it is inconsistent with the stoichiometry of
 376 exchange between two protonic sites located in the same 4-5- and 6- membered rings and
 377 one Zn^{2+} cation (2/1). The formation of the **Species II** ($\text{O}^- \text{Zn}^{2+} \text{O}^-$) should give a
 378 $[\text{LAS}]_{\text{created}}/[\text{BAS}]_{\text{neutralized}}$ ratio of 0.5. This excludes the presence of Zn^{2+} cation stabilized
 379 by two vicinal lattice Al atoms. Assuming that the main species formed are oxo-binuclear
 380 cations: $\text{O}^- \text{Zn}^{2+} \text{O}^- \text{Zn}^{2+} \text{O}^-$ (**Species III**) linked to NNN pairs of Al atoms, the ratio between
 381 the neutralized BAS and created LAS is 2/2. The difference between the theoretical values
 382 and measured values could simply be due to a problem of the quantification of the LAS.
 383 Indeed, the electronic configuration of the Zn^{2+} cation ($[\text{Ar}] 3d^{10}$) allows the coordination of
 384 two nitrogen-containing molecules (such as pyridine or ammonia). Berndt et al. concluded
 385 that the exchange of zinc ions generates Lewis-acidic sites, adsorbing two ammonia
 386 molecules. [48] The pyridine adsorption on Zn cation leads to the formation of bis(pyridine)
 387 ZnII complex (**Scheme 4**).



388

389

Scheme 4: Bis(pyridine)ZnII complex.

390 The $[\text{LAS}]_{\text{created}}/[\text{BAS}]_{\text{neutralized}}$ ratio corresponds to the measured ratio of 2 (4/2). In all
 391 the catalysts series, at least two main zinc species persist: oxo- binuclear cations ($\text{O}^- \text{Zn}^{2+} \text{O}^-$ -

392 $\text{Zn}^{2+}\text{-O}^-$) and oxide. The Zn cation can be quantified by pyridine and the amount of $(\text{ZnO})_n$
393 from the metal balance. However, it should be noted that on series 40, a slightly higher
394 amount of Lewis acid sites were measured than would be expected in taking account the
395 $[\text{LAS}]_{\text{created}}/[\text{BAS}]_{\text{neutralized}}$ of 2 (**Figure 5c**). On HZ40, some Zn^{2+} cation can be stabilized
396 by internal silanols ($\text{Al-O-Zn}^{2+}\text{-O-Si}$). The stoichiometry here is 1/1, i.e. the neutralization of
397 one Brønsted acid site yields one new Lewis acid site able to chemisorbed two pyridine
398 molecules (**Species IV**). The concentration of mononuclear Zn cation stabilized by internal
399 silanol is calculated from the difference between that of the oxo-binuclear cations drawn from
400 the neutralization of Brønsted acid sites and that of measured LAS. It should be noted that it is
401 more accurate to quantify the oxo-binuclear Zn cation (**Species III**) by the loss deficit of
402 Brønsted acid sites than by the creation of Lewis acid sites (**Table 1**). The latter may
403 underestimate their total amount due to (partially) hindered accessibility of the pyridine probe.
404 Indeed, a distortion appears for high Zn content (> 4 wt. % (**Figure 5a and 5c**).

405 The bar chart in **Figure 6** shows, for all catalyst series, the evolution of the
406 distribution of the zinc species (**III, IV and VI-VII**) as a function of metal content. The
407 impregnation of $\text{Zn}(\text{NO}_3)_2$, followed by a calcination, begins with the formation of an oxo-
408 binuclear Zn cation, and in presence of internal silanols mononuclear species also appear
409 (**Species IV**) appear. Their concentrations increase with the zinc content up to a plateau,
410 which is reached at the zeolite exchange capacity. The maximum content on species **III** is 2.8,
411 1.3 and 0.4 wt. % for series 15, 40 and 75, respectively, that for species **IV** is 0.17 wt.%. The
412 further addition of metal results in the deposition and accumulation of zinc oxide on the
413 zeolite external surface.

414 3. Catalytic performances

415 3.1. Catalytic performances of the acidic zeolites: HZ 15, 24, 40, and 75:

416 The transformation of ethylene is carried out at 500 °C under atmospheric pressure with a
417 high GHSV (13 300 h⁻¹) and diluted ethylene (0.005 MPa). **Figure 7a** shows the performance
418 of the four protonic zeolites as a function of their concentration of Brønsted acid sites. On
419 HZ40 and HZ75, less than 2% of ethylene is converted, which is apparently in direct
420 contradiction with the results of many studies [**Table SI.3**, 9, 49-55]. Indeed, generally
421 accepted mechanism of ethylene oligomerization on H-zeolites involves the olefin molecules
422 protonation by BAS and further reactions through carbenium ions (conjunct polymerization,
423 protolytic cracking). The low activity can be ascribed to the severe operating conditions that
424 were employed. Indeed, the high temperature [5, 51], low olefin partial pressure [5, 51, 53-55]
425 and short contact times limit the oligomerization reaction. For instance, on ZSM-5 (Si/Al =
426 103) at 475 °C with dilute ethylene (0.013 MPa), the conversion is only to 2% [53], whereas
427 at 350 °C and P_{C₂H₄} of 0.1 MPa, over 83% conversion was reported. [50] The performance of
428 HZ25 is consistent with what has been reported by Rosynek et al. also over a commercial H-
429 ZSM-5 zeolite (PQ corporation) with the same Si/Al ratio.[50] They obtained a conversion
430 of 40% at 520 °C with diluted ethylene (0.003 MPa) and a higher contact time. However,
431 using a same contact time as used in this study (i.e., 0.27 s), the extrapolated is expected to be
432 only 7.7%, which is in agreement with our results.

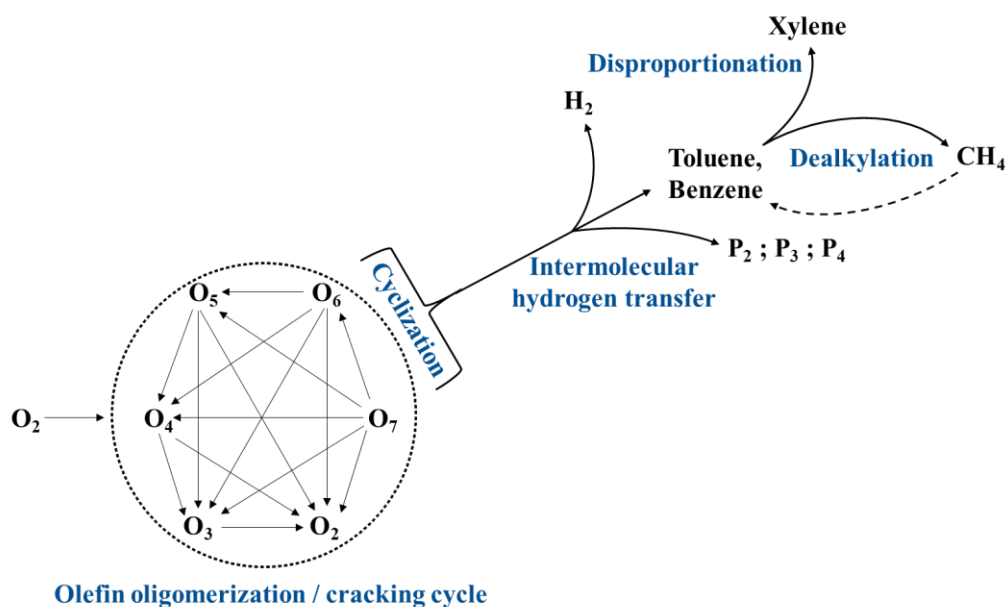
433 The conversion of ethylene is not proportional to the concentration of BAS, but increases
434 exponentially as the Si/Al ratio decreases (**Figure 7a**). The increase only appears surprisingly
435 from a large amount of BAS (~150 μmol g⁻¹). This means that the turnover frequency of
436 protonic sites changes with the Si/Al ratio. The activity enhancement, in particular on HZ15,
437 could be due to an exaltation of the strength of acid sites by the extraframework aluminum
438 species (**Figure 4**), and/or be related to a higher local concentration of reactant that is
439 adsorbed on EFAL species with Lewis acidity. [56] But, all studied samples demonstrate the
440 presence of FTIR signature at 3665 cm⁻¹ from EFAL (**Figure 1** and **Figure 3**), but the

441 catalysts performance is different. HZ25 contains more Lewis sites than HZ15 (**Table 1**), but
442 its activity in oligomerization reaction is lower (**Figure 7a**). Note, the BAS concentration is
443 higher for HZ15 and its activity is higher too. Thus, the possible involvement of EFAL
444 species in the reaction seems unlikely.

445 The results show that the intrinsic activity of protonic acid sites is not only determined by
446 their strength but also by their density or rather on the concentration of next nearest
447 neighbours pairs of Al atoms. The bimolecularity of ethylene transformation (dimerization)
448 suggests that two protonic acid sites are implied in this catalysis. As the conversion is less
449 than 1% on HZ75 despite the large quantity of BAS, the activity of the isolated protonic acid
450 sites in the transformation of ethylene is almost negligible. Thus, the conversion of ethylene
451 has been plotted as a function of the concentration of NNN pairs of Al atoms calculated from
452 the Price simulation [16]: $[PyH^+] \times \text{fraction of NNN Al}$. (**Figure 7a**). Catalyst activity is
453 proportional to the square of the concentration of NNN protonic sites. This proportionally was
454 found in various bimolecular reaction over zeolite catalysts: bimolecular butane isomerization
455 [57], alkane cracking through the carbenium ion chain mechanism [58], toluene
456 disproportionation [59], etc.

457 On HZ15, the ethylene conversion is proportional to the contact time (**Figure 7b**) even at
458 high conversion, indicating a pseudo-zero order reaction with a kinetic constant of $1.1 \cdot 10^6$
459 mol h^{-1} . As a result, only a small fraction of reactant are in contact with active site in which
460 they are able to react, and this fraction is continually replenished.

461 **Figure 8** compares the initial molar yields of H_2 , CH_4 , paraffins ($\text{P}_2\text{-P}_4$), olefins ($\text{O}_3\text{-O}_4$)
462 and aromatics (BTX) as a function of the ethylene conversion. **Scheme 3** presents a reaction
463 scheme based on products selectivity obtained on HZ15 catalyst.



464

465

Scheme 5: Reactions of ethylene on H-ZSM-5 zeolite.

466 Propylene is the main product and *iso* and *n*-butene, are "apparent" primary products.

467 Linear and branched hexene and pentene are also produced, but in low yields (<1%). These

468 olefins are obtained by an oligomerization-cracking mechanism (**Scheme 5**) which appears

469 instantaneously due to the higher reactivity of the sole primary product (i.e. *n*-butene) than for

470 the reactant.

471 Methane, benzene and toluene, appear simultaneously as secondary products from a

472 conversion of 7% (extrapolated value), indicating that dealkylation of toluene occurs at 500

473 °C. CH₄ could also be produced by α -scission of olefins. Yet, such monomolecular cracking,

474 which requires very strong acid sites [59], is expected to lead concomitantly to the formation

475 of methane and olefins, and hence CH₄ should appear as an apparent primary product. As this

476 is not the case, CH₄ is mainly produced by dealkylation of toluene (**Scheme 5**).

477 Xylenes are ternary products appearing at ca 50% conversion, probably produced by the

478 toluene disproportionation. This bimolecular reaction, which is catalysed by strong Brønsted

479 acid sites associated with extra-framework aluminium species, requires a relatively high

480 partial pressure of toluene. [60-61] It is noteworthy, that no particular para-selectivity is

481 observed, despite of the use of the ZSM-5 zeolite. The concomitant formation of aromatics,

482 hydrogen and paraffins indicates that involvement of two mechanisms: intra-molecular
483 dehydrogenation (DH) and inter-molecular hydrogen transfer (HT) (**Scheme 5**). Selectivity to
484 HT has been correlated with the fraction of pair Al sites estimated by a statistical calculation
485 [48], and is favoured by a high density acid sites. The dehydrogenation of cycloalkanes leads
486 to a molar ratio of H₂ to aromatics of 3: $C_6H_{12} \rightleftharpoons C_6H_6 + 3H_2$, and the intermolecular
487 hydrogen transfer with olefins to a molar ratio of paraffins to aromatics of 3: $C_6H_{12} +$
488 $C_3H_6 \rightleftharpoons C_6H_6 + 3C_3H_{12}$. The proportion of the two mechanisms (molar ratio of paraffins to
489 hydrogen) depends on the yield into aromatics due to the molecularity of the hydrogen
490 transfer; HT and HD occur in the same proportion for a low BTX yield (3.4%), passing from
491 2.4 to double the yield.

492 Recently, Uslamin et al. are proposed, based on isotope labelling experiments, that
493 mechanism of ethylene conversion on H-ZSM-5 shares similarities with the dual-cycle
494 hydrocarbon pool mechanisms.[5] They shown that the intermediate species retained can
495 contribute to the activation of ethylene *via* their alkylation, but in our case the data are
496 analysed after only 10 min. of reaction and the quantity of coke retained is extremely low,
497 below the detection limit (0.5wt%).

498 **3.2. Catalytic performances of the bifunctional catalysts: series 15, 40 and 75**

499 ZnO, HZ40 and HZ75 are inactive at 500 °C in the transformation of dilute ethylene.
500 However, the wet impregnation of zinc on zeolite results in an increase of the conversion
501 (**Figure 9a**). This suggests that under severe operating conditions of low ethylene partial
502 pressure, high temperature and high GHSV, the oxo-binuclear Zn cation species are active at
503 least in the dimerization of ethylene. Conversion increases with Zn content, despite the loss of
504 BAS concentration (**Figure 9b**), until a plateau is reached that depends on the acidity of the
505 protonic zeolite (**Figure 9a**). The higher the Si/Al, the lower the maximum conversion. But
506 for the HZ15 zeolite, already active in the transformation of ethylene, the zinc deposit causes

507 a significant decrease in conversion, then increases with the Zn content until it reaches a
508 plateau.

509 The gain in activity does not correlate with the concentration of Brønsted acid sites, but
510 with that of the oxo-binuclear Zn species (**Species III**). A low content of Zn is sufficient to
511 switch from the acid-catalyzed mechanism to the metal-catalyzed pathway. The conversion
512 on series 15 and 75 is proportional to the concentration of **species II** and follows the same
513 slope (**Figure 9c**). However, the conversion in series 40 is higher, meaning that the
514 mononuclear Zn cations stabilized by the internal silanol (**Species IV**) are also active in the
515 transformation of ethylene.

516 2.1Zn40 catalyst appears to be less active in the transformation of ethylene than HZ15
517 zeolite, for which the active sites are the pair of Brønsted acid sites (**Figure 7c**). Hence, the
518 initial decline in activity of HZ15 after the addition of Zn is consistent with the neutralization
519 of the very active pair aluminium atoms. In addition, the apparent kinetic order is different on
520 the two catalysts (**Figure 7b**). Indeed, on 2.1Zn40 the plot of $\ln(1-X)$ as a function of contact
521 time gives a straight line through the origin, indicating a pseudo first-order reaction with a
522 kinetic constant of $5.7 \times 10^3 \text{ h}^{-1}$ (**Figure SI.14**).

523 Regardless of the method used for Zn loading, its presence completely changes the
524 selectivity of acid catalyst. C_4H_8 clearly is a primary product, while CH_4 , C_3H_6 , H_2 and
525 aromatics composed of benzene (B), toluene (T) and also xylene (X) and ethylbenzene (EB),
526 are secondary products. These products could be considered practically as primary products
527 (**Figure 8**) because they are produced simultaneously from a very low conversion, ca 2%
528 (extrapolated value).

529 .Hydrogen resulting from the dehydrogenation of naphthenes or olefinic naphthenes is
530 also consumed at high conversion through the hydrogenation of olefins into light alkanes
531 (mainly ethylene into ethane). The hydrogenating activity of Zn-based catalysts was studied

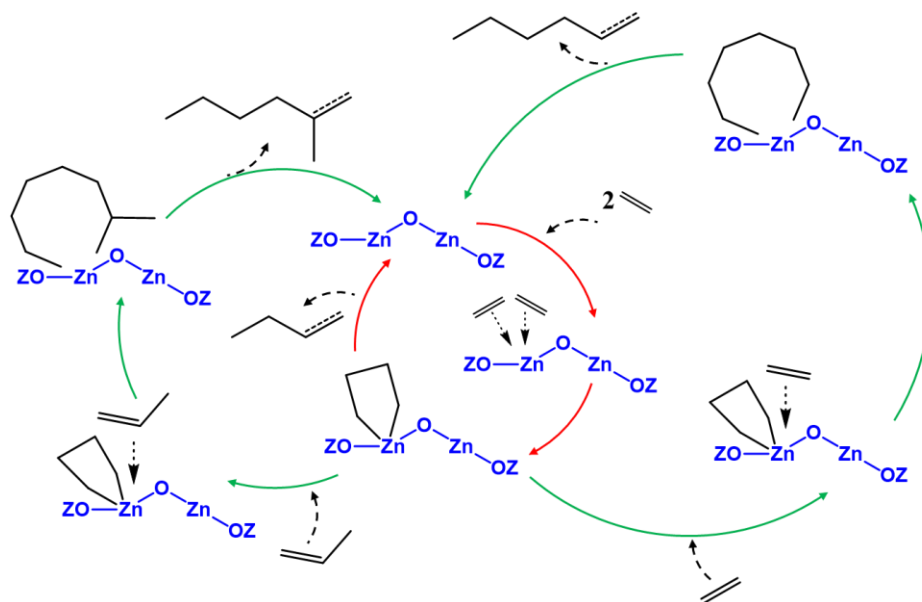
532 by conducting experiments with an equimolar mixture of C₂H₄/H₂ (5.3 kPa/5.3 kPa) on
533 catalysts having the species: i) **II** and **III** (0.8 Zn₄₀ and 2.0 Zn₁₅) and ii) **II**, **III**, **VI** and **VII**
534 (2.1 Zn₄₀ and 8.1 Zn₁₅). (**Figure 6**). All catalysts are active in ethylene hydrogenation,
535 suggesting that the hydrogenating activity of ZnO is significantly lower than this of Zn cation.
536 Higher metallic/Lewis acid site sites results to higher hydrogenation rates (**Figure SI. 13**),
537 which is consistent with Mehdad et al. [25]. Functional density theory has shown that
538 recombinant hydrogen desorption is easier on the Zn site stabilized by two framework Al
539 atoms (species **II**) than on oxygen-bridged zinc sites (**species III**) [40], suggesting different
540 hydrogenating activity on these two sites

541 The presence of hydrogen in the feed gas causes both an increase of the ethane yield and
542 a decrease in aromatics formation (**Figure SI.13**). The hydrogenation of ethylene has a direct
543 impact on aromatics yield, which is limited or even decreased when a large portion of
544 ethylene is hydrogenated. The lower the partial pressure of the olefins, the lower the
545 aromatics yield. Therefore, hydrogen should be removed from the reactor, which might be
546 achieved through the use of catalytic membrane, in order to improve the performance of the
547 dilute dry gas aromatization process. Toluene (T) and benzene (B) are the main aromatics
548 products and are formed in the same proportions regardless of the conversion, contrary to what
549 is observed with acid catalysts (**Figure 8**). The benzene formation is not the result of the
550 dealkylation of toluene, as the very “strong” acid sites necessary for this reaction have
551 disappeared after zinc impregnation (**Figure 4**). A T/B molar ratio of one has already been
552 obtained by Biscardi et al. in the conversion of propane on Zn/H-ZSM-5 at 500 °C. [28] The
553 authors assume that benzene and toluene are formed from a common pool of alkene
554 intermediates [27] and the T/B molar ratios was an accurate measure of the average size of the
555 alkenes in this pool. However, the toluene/benzene molar ratios are different on the acid
556 catalysts than on the bifunctional catalysts. This would imply that the oligomerization-

557 cracking acid mechanism is influenced by the presence of the Zn-LAS, or that the olefins
558 oligomerization occurred more rapidly on the metal cation. A further argument for the
559 oligomerization of olefins over Zn cations, is the concomitant formation of aromatics at 6, 7
560 and 8 carbon atoms (A₆-A₈). The neutralization of the strongest acid sites by the Zn cation
561 combined with a low partial pressure of toluene (especially at low conversion) is a strong
562 argument that xylene do not result from the disproportionation of toluene. Xylenes are likely
563 to be produced by the isomerization of ethylbenzene (EB), which requires weaker acid sites
564 than the disproportionation [60-61], and is therefore rapid at 500 °C. Consequently, the yield
565 into EB is low (~0.4 mol. %). Styrene, present in lower amount, appears at a higher
566 conversion (**10%, Figure 8**), and is produced by dehydrogenation of the ethyl group. There
567 are two potential pathways for the formation of EB, either by alkylation of benzene with ethyl
568 carbenium ions (unfavourable at high temperature), or by a cyclization-dehydrogenation of
569 octane/octadiene. The latter route suggests a new mode of olefin formation, different from the
570 conventional oligomerization-cracking mechanism. The greater the length of the carbon
571 chain, the higher the sensitivity to cracking by β -scission. The high reactivity of octene to
572 cracking does not therefore make it possible to obtain a relatively high yield into A₈ (**Figure**
573 **8**) by conventional bifunctional catalysis (oligo-cracking-cyclization on acid sites and
574 dehydrogenation on metal sites). As proposed by Lobo et al., Zn in the form of Lewis acid
575 sites can oligomerize ethylene successively *via* the Cossee-Arman mechanism. [25] This
576 mechanism involves an intermediate coordination complex that contains both the growing
577 oligomer chain and ethylene. These ligands combine within the coordination sphere of the
578 metal to form a polymer chain which is elongated by two carbon atoms (**Scheme SI.1**).
579 Ethylene is also most likely oligomerized *by* a metallacyclic mechanism such as on a Philips
580 polymerization catalyst (Cr/SiO₂). [63] Indeed, two molecules of ethylene are able to
581 coordinate to the vacant coordination sphere of the Zn active site and form a zinco-

582 cyclopentane ring (**Scheme 6**). Two routes are possible, either via β -H transfer and release of
 583 but-1-ene, or through the coordination and insertion of another ethylene (or propylene which
 584 results from the hydrogenolysis of n-butene) to form a zinco-cycloheptane (or -cyclooctane)
 585 ring. Steric constraints lead to desorption of C_6H_{12} as well as, the regeneration of active site.
 586 A highly reactive olefin molecule diffuses to the BAS to cycle into naphthenes which
 587 dehydrogenate into aromatic molecules on a cationic Zn site.

588 The hydrogenation rate increases with the partial pressure of hydrogen, and seems to be
 589 favoured by the presence of the monomolecular Zn-LAS species. Hydrogenation could also
 590 be due the presence of nanoclusters of ZnO as proposed by Mehdad et al. [25]



591

592 **Scheme 6:** Metallacyclic mechanism for ethylene di and trimerization.

593 **Figure 10** shows the molar yields of all products as a function of the content of oxo-
 594 binuclear Zn cation ($O^-Zn^{2+}-O-Zn^{2+}-O^-$, **Species III**). The formations of methane, ethane and
 595 hydrogen occur at a lower conversion on the series 40, while the yields of olefins (O_3-O_4) and
 596 aromatics (BTX, EB, S) are similar on all three catalyst series. Consequently, selectivity
 597 depends on the nature of the Zn Lewis acid site. The mononuclear Zn cations stabilized by the
 598 internal silanol (**species IV**) catalyse only hydrogenolysis and hydrogenation reactions and the

599 oxobinuclear Zn cations catalyze the dimerization of ethylene. The higher activity on the
600 series 40 is only due to the presence of hydrogenolysis and hydrogenation reactions.

601 **Conclusion**

602 The aromatization mechanism of light alkanes on Zn/H-MFI is accepted by the
603 scientific community as bifunctional, which is initiated on the Zn species by dehydrogenation
604 reaction of the alkanes (rate limiting-step), followed by oligomerization-cyclization of the
605 desorbed olefin on acid sites, and terminated on the Zn species by dehydrogenation of the
606 naphthenes. This bifunctional mechanism seems possible using propane/propene, as
607 secondary intermediate carbenium ion are involved. However, as far as ethylene is concerned,
608 the corresponding carbenium ions are primary and therefore the classical bifunctional
609 mechanism becomes unlikely, especially under harsh operating conditions. The intrinsic
610 activity of protonic acid sites in ethylene transformation depends on their density or rather on
611 the concentration of next nearest neighbours pairs of Al atoms. The isolated Al atoms can be
612 considered almost inactive in the dimerisation of ethylene. Butenes are rapidly converted on
613 Brønsted acid pairs sites, resulting in a well-balanced oligomerization-cracking pool.
614 Aromatics are obtained through a hydrogen transfer with olefins, or by dehydrogenation of
615 cycloalkanes made possible by the EFAL species.

616 A small amount of Zn Lewis acid sites is sufficient to completely alter the kinetic and
617 selectivity. The particular selectivity with the formation of styrene, ethylbenzene and toluene
618 and benzene with a molar ratio of 1, indicates that the transformation of ethylene takes place
619 by a new mechanism. The dimerization occurs *via* a metallacyclic mechanism by the
620 formation of cyclobutyl-zinc intermediate and the growth of the carbon chain occurs, through
621 the opening of cyclo-organozinc species. The desorbed products are olefins which cyclize
622 easily into naphthenes on Brønsted acid sites. But this dual sites can also absorb hydrogen,
623 leading to hydrogenolysis and mainly hydrogenation reactions. Therefore, the management of

624 hydrogen production appears to be a crucial issue for the development of the process of the
625 aromatization of dilute ethylene using Zn/H-ZSM-5 catalysts.

626 This structure-reactivity study allowed to identify the active sites responsible of the
627 formation of observed products. Spectroscopic studies should be carried out to support the
628 mechanism proposal and further studies also should focus on the optimisation of catalytic site
629 and the understanding of the deactivation mechanism(s).

630 **Acknowledgment**

631 The authors gratefully acknowledge IFPEN for the financial support. The authors
632 acknowledge financial support from the European Union (ERDF) and "Région Nouvelle
633 Aquitaine". Aurelien Bonnin thanks "Ministère de l'enseignement supérieur, de la recherche
634 et de l'innovation" for Ph.D. grant.

635

636 **References**

- 637 [1] The future of Petrochemicals, towards more sustainable plastics and fertilizers,
638 www.iea.org/t&c/
- 639 [2] C.P. Nicholas, Process for oligomerizing dilute ethylene Patent (2013) 8,748,682.
- 640 [3] C. Kothari, and H. Lukoma, Benzene/Toluene, P.E.R. Planning, Editor. 2015, Nexant.
641 p. 64.
- 642 [4] H. Coqueblin, A. Richard, D. Uzio, L. Pinard, Y. Pouilloux, F. Epron, Catal. Today,
643 289 (2017) 62-69.
- 644 [5] E. A. Uslamin, H. Saito, N. Kosinov, E. Pidko, Y. Sekine E. J. M. Hensen, Catal. Sci.
645 Technol, 10 (2020) 2774-2785.
- 646 [6] Y. Xiang, H.Wang, J. Cheng, J. Matsubu, Catal. Sci. Technol., 8 (2018) 1500-1516.
- 647 [7] B. Wan, H. Chu, J. Chem Soc. Faraday Trans. 88 (1992) 2943-2947.
- 648 [8] A. Hagen, K. -H Hallmeier, C. Henning, R. Szargan, T. Inui, F. Roessner, Stud. Surf.
649 Sci. Cat. 94 (1995) 94 195-202.

- 650 [9] X. Chen, M. Dong, X. Niu, K. Wang, G. Chen, W. Fan, J. Wang, Z. Qin, *Chin. J.*
651 *Catal.* 36 (2015) 880-888.
- 652 [10] S. Tamiyakul, T. Sooknoi, L. L. Lobban, S. Jongpatiwut, *Appl. Catal. A: Gen.* 525
653 (2016) 190-196.
- 654 [11] X. Niu, J. Gao, Q. Miao, M. Dong, G. Wang, W. Fan, A. Qin, *Micro. Meso. Mat.*, 197
655 (2014) 252-261.
- 656 [12] Y. Jia, J. Wang, K. Zhang, W. Feng, S. Liu, C. Ding, P. Liu, P., *J. En. Chem.* 26
657 (2017), 540-548.
- 658 [13] X. Niu, J. Gao, K. Wang, Q. Miao, M. Dong, G. Wang, W.; Fan, Z. Qin, J. Wang, J.
659 *Fuel Process. Tech.* 157 (2017) 99-107.
- 660 [14] H. Berndt, G. Lietz, J. Völter, J., *Appl. Catal. A: Gen.* 146 (1996) 365-379.
- 661 [15] J. A. Biscardi, G. D. Meitzner, E. Iglesia, *J. Catal.*,179 (1998), 192-202.
- 662 [16] M. J. Rice, A. K. Chakraborty, A. T. Bell, *J. Catal.* 186 (1999) 222-227.
- 663 [17] E. M. El-Malki, R. A. van Santen, W. M. H. Sachtler, *J. Phys. Chem B* 103 (1999),
664 4611-4622.
- 665 [18] L. Lin, X. Zhang, N. He, J. Liu, Q. Xin, H. Guo, *Catalysts* 9 (2019) 100-115.
- 666 [19] V. B. Kasansky, A. I. Serykh, *Phys. Chem. Chem. Phys.* 6 (2004) 3760-3764.
- 667 [20] V. B. Kasansky, A. I. Serykh, B. G. Anderson, R. A van Santen, R, *Catal. Lett.* 88
668 (2003) 211-217.
- 669 [21] M. Haase, H. Welter, A. Henglein, *J. Phys. Chem.*92 (1988) 482-487.
- 670 [22] I. E. Brus, *J. Phys Chem.* 90 (1986) 2555-2560.
- 671 [23] J. Chen, Z. Feng, P. Ying, C. Li, *J. Phys Chem. B.* 108 (2004) 12669-12676.
- 672 [24] S. Bordiga, C. Lamberti, G. Ricchiardi, L. Regli, F. Bonino, A; Damin, K. P. Lillerud,
673 M. Bjorgen, A. Zecchina, *Chem. Commun.* 20 (2004) 2300-2301.
- 674 [25] A. Mehdad, R. F. Lobo, *Catal. Sci. Technol.*7 (2017) 3562-3572.

- 675 [26] E. Iglesia, J. E. Baumgartner, G. L. Price, *J. Catal.* 134 (1992) 549-571.
- 676 [27] J. A. Biscardi, E. Iglesia, *Catal. Today*, 31 (1996) 207-231.
- 677 [28] J. A. Biscardi, E. Iglesia, *J. Catal.* 182 (1999) 182, 117-128.
- 678 [29] Y. Ono, *Catal. Rev.: Sci. Eng.* 34 (1992) 179-226.
- 679 [30] A. A. Gabrienko, S. S. Arzumanov, A. V. Toktarev, D. Freude, J. Haase, A. G.
680 Stepanov. *J. Phys. Chem. C.* 123 (2019) 27573-27583.
- 681 [31] S. Arzumanov, A. Gabrienko, A. Toktarev, D. Freude, J. Haase, A. G. Stepanov, J.
682 *Phys Chem. C* 123 (2019) 3047-30485.
- 683 [32] C. Miranda, A. Ramírez, A. Sachse, P. Gaudin, Y. Pouilloux, L. Pinard, *J. Catal.* 307
684 (2018) 249-260.
- 685 [33] I. Batonneau-Gener, A. Sachse, *J. Phys. Chem. C* 123 (2019) 4235-4224.
- 686 [34] A. Zecchina, S. Bordiga, G. Spoto, L. Marchese, G. Petrini, G. Leofanti, M.
687 Padovan, *J. Phys. Chem.* 96 (1992) 498-4990.
- 688 [35] M. Abdolrahmani, K. Chen, J. L. White, *J. Phys. Chem. C* 122 (2018) 15520-15528.
- 689 [36] A. A. Gabrienko, I. G. Danilova, S. S. Arzumanov, L. V. Pirutko, D. Freude, A. G.
690 Stepanov, *J. Phys. Chem. C.*122 (2018) 25386-25395.
- 691 [37] B. H. Chiche, F. Fajula, E. Garrone, *J. Catal.* 146 (1994) 460-467.
- 692 [38] M. V. Frash, R. A. van Santen, *Phys. Chem. Chem. Phys.*2 (2000) 1085-1089.
- 693 [39] L. A. M. M. Barbosa, R. A. van Santen, *J. Mol Catal. A: Chem.* 166 (2001) 101-121.
- 694 [40] E. A., Pidko, R. A. van Santen, , *J. Phys. Chem. C* 111 (2007) 2643-2655.
- 695 [41] I. I. Ivanova, Y. G. Kolyagin, V. V. Ordonsky, E. V.; Asacheko, E. M. Pasyukova, Y.
696 A. Pirogov, *J. Mol Catal. A: Chem.*305 (2009) 47-53.
- 697 [42] R. Kokes, *Acc. Chem. Res.*, 6 (1973) 226-233.
- 698 [43] Y. Zhang, Y. Zhou, L. Huang, S. Zhou, X. Sheng, Q. Wang, C. Zhang, *Chem. Eng.*
699 *Jour.* 270 (2015) 352-361.

- 700 [44] E. B. Clatworthy, S. V. Konnov, F. Dubray, N. Nesterenko, J-P. Gilson, S. Mintova.
701 Angew. Chem. Int. Ed. 59 (2020) 19414-19432.
- 702 [45] S. V. Konnov, F. Dubray, E. B. Clatworthy, C. Kouvatas, J-P. Gilson, J-P. Dath, D.
703 Minoux, C. Aquino, V. Valtchev, S. Moldovan, S. Koneti, N. Nesterenko, S. Mintova.
704 Angew. Chem. Int. Ed. 59 (2020) 19553-19560.
- 705 [46] L. Rodriguez-Gonzalez, F. Hermes, M. Bertmer, E. Rodriguez-Castello, A. Jimenez-
706 Lopez, U. Simon. Appl. Catal. A. Gen. 328 (2007) 174-182.
- 707 [47] J. Penzien, A. Abraham, J.A. van Bokhoven, A. Jentys, T. E. Müller, C. Siervers, J. A.
708 Lercher, J. Phys. Chem. B. 108 (2004) 4116.-4126.
- 709 [48] H. Berndt, G. Lietz, B. Lücke, J. Völter, Appl. Catal. A: Gen. 146 (1996) 351-363.
- 710 [49] K. Arishtirova, C; Dimitrov, K. Dyrek, K. -Hz Hallmeier, Z. Popova, S. Witowski, ,
711 Appl. Catal. 81 (1992) 15-26.
- 712 [50] P. Qiu, J. H. Lunsford, M. P. Rosynek, Catal. Lett. 52 (1998) 37-42.
- 713 [51] L. A. Dufresne, R. Le Van Mao, Catal. Lett. 25 (1994) 371-383.
- 714 [52] R. Le van Mao, L. A. Dufresne, J. Yao, Y. Yu, Appl. Catal. A : Gen 164 (1997) 81-
715 89.
- 716 [53] J. Gao, C. Wei, M. Dong, G. Wang, Z. Li, Z. Qin, J. Wang, W. Fan, ChemCatChem
717 11 (2019) 3892-3902.
- 718 [54] L. Ying, J. Zhu, Y. Cheng, L. Wang, X. Li, J. Ind. Eng. Chem.33 (2016) 80.-90.
- 719 [55] D. B. Lukyanov, Stud. Surf. Sci. Catal. 122 (1999) 299-306.
- 720 [56] J. A. Bokhoven, M. Tromp, D. C. Koningberger, J. T. Miller, J. A. Z. Pietrese, J. A.
721 Lercher, B. A. Williams, H. H. Kung, J. Catal. 202 (2001) 129-140.
- 722 [57] C. Bearez, F. Chevalier, M. Guisnet, Kinetic study. React. Kinet. Catal. Lett.,22
723 (1983) 405-409.
- 724 [58] G. Giannetto, M. Guisnet, J. Chem. Soc. Chem. Commun., 1986, 1302-1303.

- 725 [59] N.S. Gnep, M. Guisnet *Appl. Catal.* 1 (1981) 329-342.
- 726 [60] M. Guisnet, L. Pinard, *Catal. Rev.* 60 (2018) 337-437.
- 727 [61] J.A. Lercher, A. Jentys, A. Brait, Catalytic test reactions for probing the acidity and
 728 basicity of zeolites, In *Mol Sieves*; Karge, H. G., Weitkamp, J., Eds.; Springer, 2008;
 729 Vol. 6, pp 153–212.
- 730 [62] D. Cicmil, I.K. van Ravenhorst, J. Meeuwissen, A. Vantomme, B. M. Weckhuysen,
 731 *Catal. Sci. Technol.* 6 (2016) 731-743.

734 **Table and figure Captions**

- 735
- 736 Table 1: Zn content and concentration of Brønsted and Lewis acid sites on the three
 737 catalyst series.
- 738 Figure 1: IR spectra of (a) OH region and (b) pyridine coordinated to Lewis acid sites on
 739 the protonic zeolites with molar Si/Al ratio of 15, 25, 40, and 75. In the
 740 presented spectra, the adsorbance was normalized to sample wafer density (g cm^{-2}).
 741
- 742 Figure 2: Micropore volume as a function of zinc content on catalyst series 15 (\square), 40
 743 (Δ) and 75 (\circ). (Full and open symbols = HZ and Zn based catalysts,
 744 respectively).
- 745 Figure 3: FT-IR spectra of OH region as a function of zinc content on catalyst series 15,
 746 40 and 75 (dashed line = HZ catalysts). In the presented spectra, the
 747 adsorbance was normalized to sample wafer density (g cm^{-2}).
- 748 Figure 4: NH_3 -TPD profiles as a function of zinc content on catalyst series 15, 40 and 75
 749 (dashed line = HZ zeolites).
- 750 Figure 5: Concentrations of neutralized Brønsted acid sites (a) and formed Lewis acid
 751 sites (b) as a function of Zn content. (c) Stoichiometry of the transformation of
 752 BAS into LAS by Zn impregnation. (blue symbol: $.8\text{Zn}40^{\text{IE}}$ green symbol :
 753 $0.8\text{Zn}40^{\text{DI}}$, and full symbol data from [8]).
- 754 Figure 6: Bar chart of the molar distribution of the Zn species on catalyst series 15, 40
 755 and 75.

- 756 Figure 7: Light olefins conversion on protonic zeolites:
757 (a) Ethylene conversion as a function of concentration of BAS (black symbol)
758 and pair of BAS (red symbol).
759 (b) Ethylene conversion as a function of contact time on HZ15 (blue symbol)
760 and 2.1Zn40 (red symbol).
- 761 Figure 8: Molar yields of H₂, CH₄, paraffins: C₂-C₄ olefins: O₃-O₄ and aromatics: BTX,
762 EB and styrene as a function of the conversion.
- 763 Figure 9: Ethylene conversion as a function of impregnated zinc content (a),
764 concentration of Brønsted acid sites (b) and content of oxo-binuclear Zn cation.
765 (Operating condition: 500 °C, P= 1 atm, τ= 0.27 s).
- 766 Figure 10: Molar yields of the products of ethylene transformation as a function of the
767 content of oxo-binuclear Zn cation.

Supporting Information

- 770 Table SI.1: Properties of commercial zeolites HZSM-5: 15, 25, 40 and 75.
- 771 Table SI.2: Impact of pretreatment on conversion and products selectivity obtained at 500
772 °C on 2.1Zn40.
- 773 Table SI.3: Operating conditions used in the open literature for ethene oligomerization on
774 HZSM-5 catalyst.
- 775 Figure SI.1: Probability of NNN pairs of Al atoms able to stabilize a divalent cation, and to
776 form an oxo-binuclear cation drawn from stochastic simulation of Rice et al.
777 [14].
- 778 Figure SI. 2: Integrated adsorbance determined for pyridine adsorption on MFI (Si/Al =27)
779 and α-Al₂O₃.
- 780 Figure SI.3: Nitrogen sorption at -196 °C of the protonic zeolites with molar Si/Al ratio of
781 15, 25, 40, and 75.
- 782 Figure SI.4: TEM images of commercial zeolites.
- 783 Figure SI.5: ²⁷Al NMR spectrum of HZ40, 2.1Zn15 and 5.6Zn15 catalysts.
- 784 Figure SI.6: FT-IR spectra of OH region HZ15 zeolite before (full line) and after (dashed
785 line) pyridine adsorption at 150 °C.
- 786 Figure SI.7: Figure SI.7: XRD spectra of HZ40 (green), 2.1Zn40 (blue) and 3.6Zn40
787 (black).

788 Figure SI.8: FT-IR spectra of OH region of Zn based catalysts prepared by wet (WI) and
789 dry impregnation (DI) and ion exchange (IE). In the presented spectra, the
790 adsorbance was normalized to sample wafer density (g cm^{-2}).

791 Figure SI. 9: UV-visible DRS spectra of catalysts series 40.

792 Figure SI. 10: TEM images of bifunctional catalysts with a lower and higher metal content
793 than the Zn exchange capacity.

794 Figure SI. 11: FT-IR spectra of pyridine adsorption on 15, 40 and 75 catalyst series. In the
795 presented spectra, the adsorbance was normalized to sample wafer density (g
796 cm^{-2}).

797 Figure SI.12: Integrated intensity of Si-O(H)-Al band vs the concentration of Brønsted acid
798 sites probed by pyridine at 150 °C.

799 Figure SI.13: Molar yields into (a) ethane and (b) aromatics as a function of the conversion,
800 and (c) molar yield into ethane as a function of the content of oxo-binuclear Zn
801 cation with (in red) and without (in black) of hydrogen (5 vol. %) in the feed
802 gas.

803 Figure SI.14: Test for the first-order rate equation: $-\ln(1 - X_A) = k\tau$ on 2.1Zn40.

804 Scheme SI.1: Reaction scheme of the ethylene transformation at 500 °C on bifunctional Zn-
805 HZSM-5 catalyst through a Cossee-Arlman mechanism.

Table 1: Zn content and concentration of Brønsted and Lewis acid sites on the three catalyst series.

Series	Catalyst ^a wt. %	Zn/Al ^a mol/mol	[PyH ⁺] ^b μmol g ⁻¹	[PyL] ^c	ZnO ^d nm
15	HZ15	-	515 (1041)	44	
	0.7Zn15	0.3	364	346	
	2.0Zn15	0.3	201	671	0.0
	3.4Zn15	0.5	144	792	
	4.1Zn15	0.6	121	688	6.8
25	8.1Zn15	1.2	84	655	
	HZ25	-	307 (640)	54	
40	HZ40	-	286 (386)	28	
	0.5Zn40	0.2	229	176	
	0.8Zn40	0.3	217	253	
	0.8Zn40 ^{IE}	0.2	198	189	
	0.8Zn40 ^{DI}	0.3	175	212	
	1.4Zn40	0.5	199	329	
	2.1Zn40	0.7	163	367	0.0
	3.6Zn40	1.3	77	399	9.1
	5.6Zn40	1.8	100	443	
75	HZ75	-	148 (219)	21	
	0.3Zn75	0.2	111	67	0.0
	0.7Zn75	0.4	92	98	
	2.7Zn75	1.6	84	102	14.8

^a = Zn content measured by ICP analysis, ^{b,c} = concentrations of Brønsted and Lewis acid sites probed by thermodesorption of pyridine at 150 °C.
^d = measured on MET images. In bracket theoretical acidity calculated from Al content.

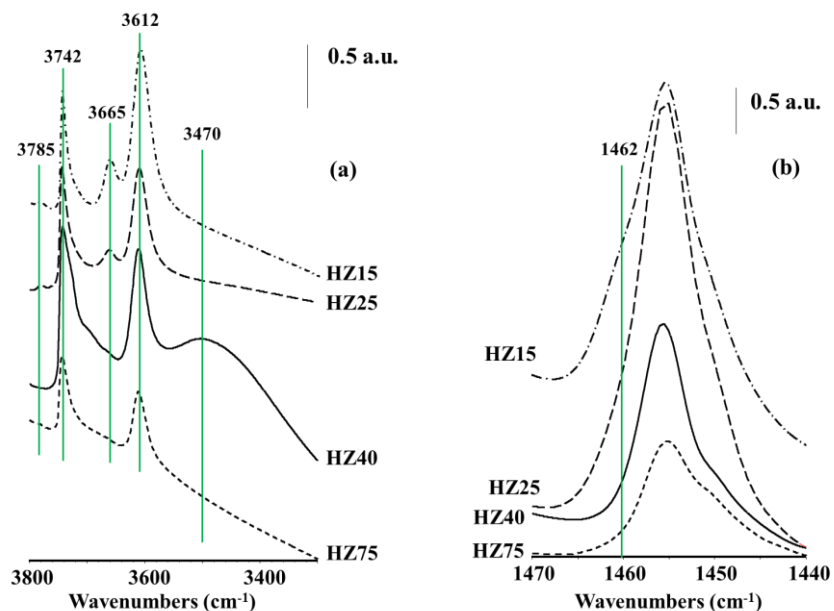


Figure 1: IR spectra of (a) OH region and (b) pyridine coordinated to Lewis acid sites on the protonic zeolites with molar Si/Al ratio of 15, 25, 40, and 75. In the presented spectra, the adsorbance was normalized to sample wafer density (g cm^{-2}).

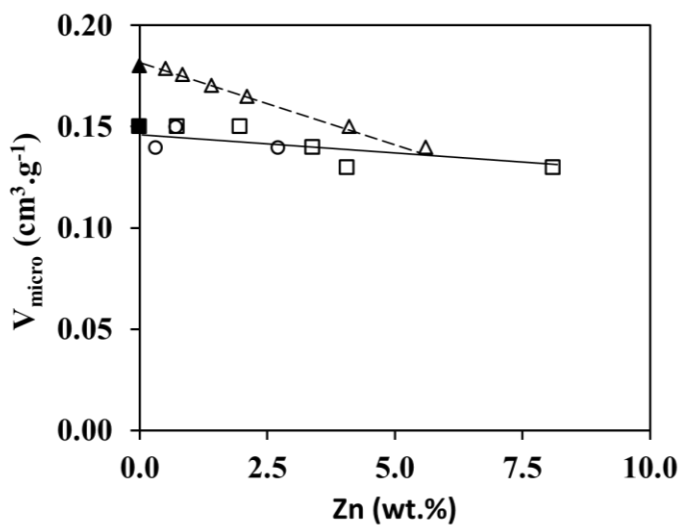


Figure 2: Microporous volume as a function of zinc content on 15 (□), 40 (Δ) and 75 (○) catalyst series. (Full and open symbols = HZ and Zn based catalysts, respectively).

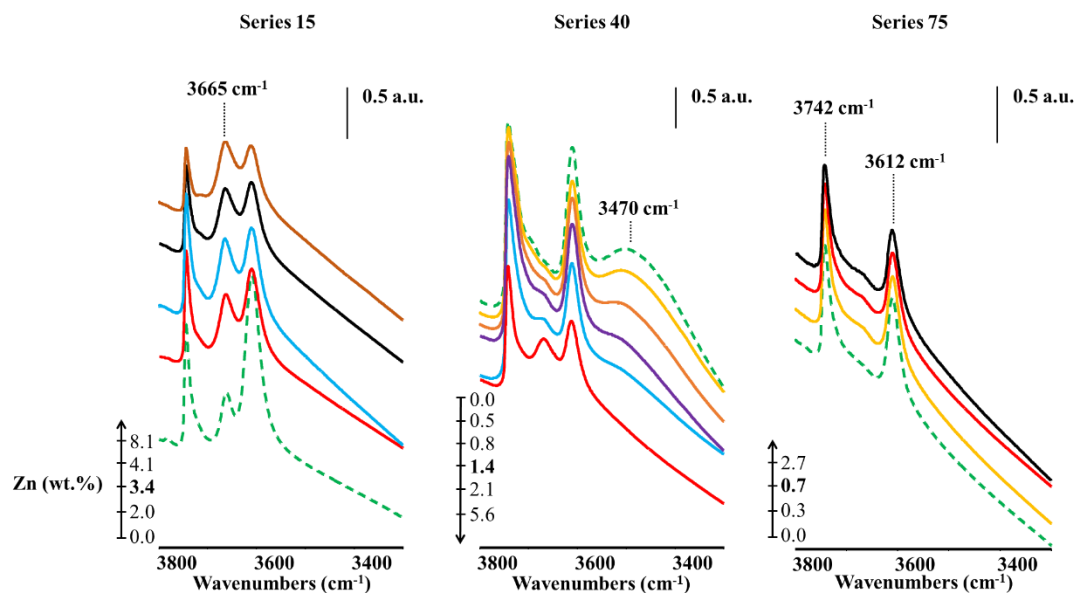


Figure 3: IR spectra of OH region as a function of zinc content on 15, 40 and 75 catalyst series (dashed line = HZ catalysts). In the presented spectra, the adsorbance was normalized to sample wafer density (g cm^{-2}).

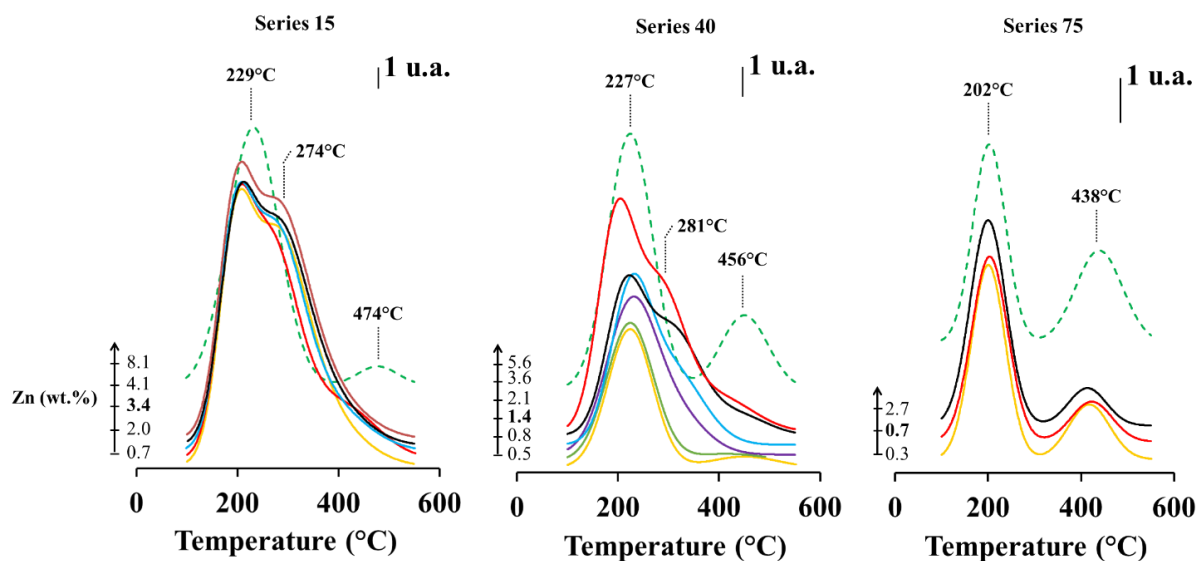


Figure 4: NH_3 -TPD profiles as a function of zinc content on 15, 40 and 75 catalyst series (dashed line = HZ zeolites).

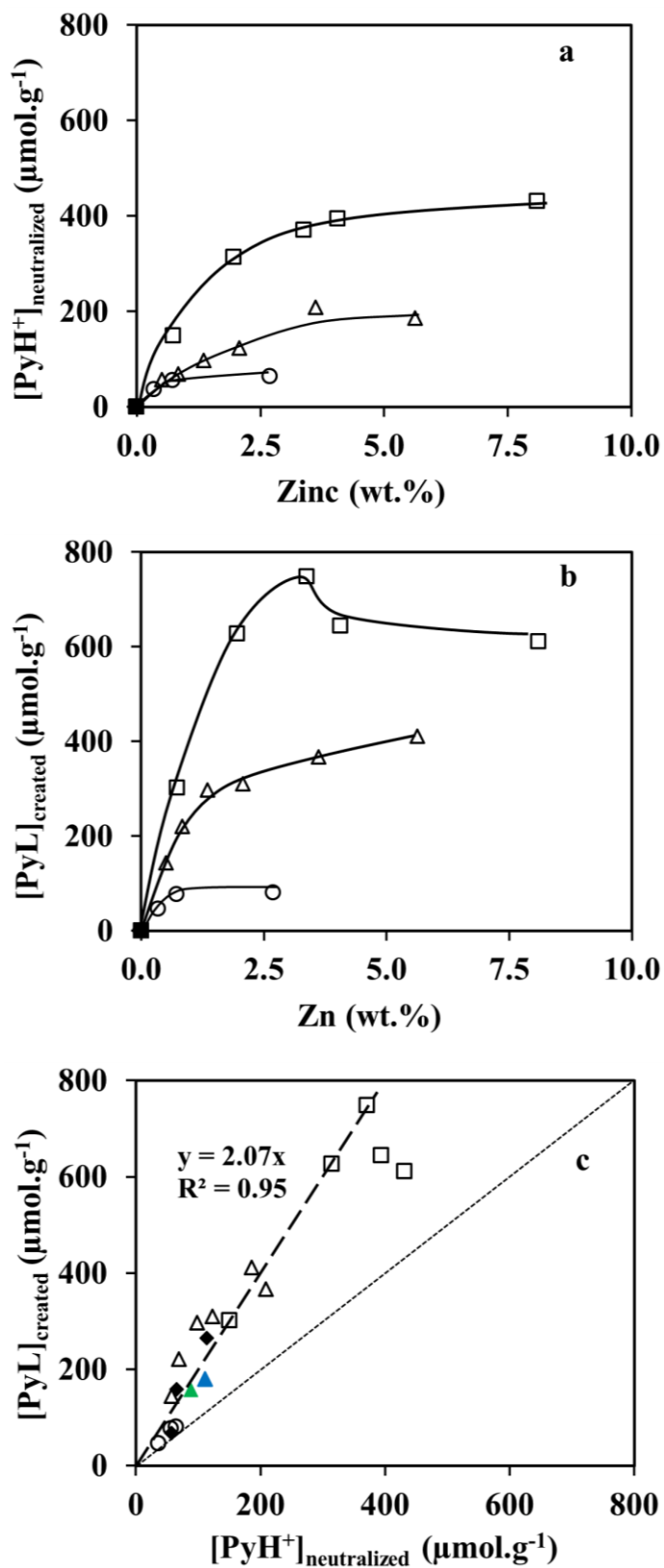


Figure 5: Concentrations of neutralized Brønsted acid sites (a) and formed Lewis acid sites (b) as a function of Zn content. (c) Stoichiometry of the transformation of BAS into LAS by Zn impregnation. (Blue symbol: $.8\text{Zn}40^{\text{IE}}$ green symbol: $0.8\text{Zn}40^{\text{DI}}$, and full symbol data from [8]).

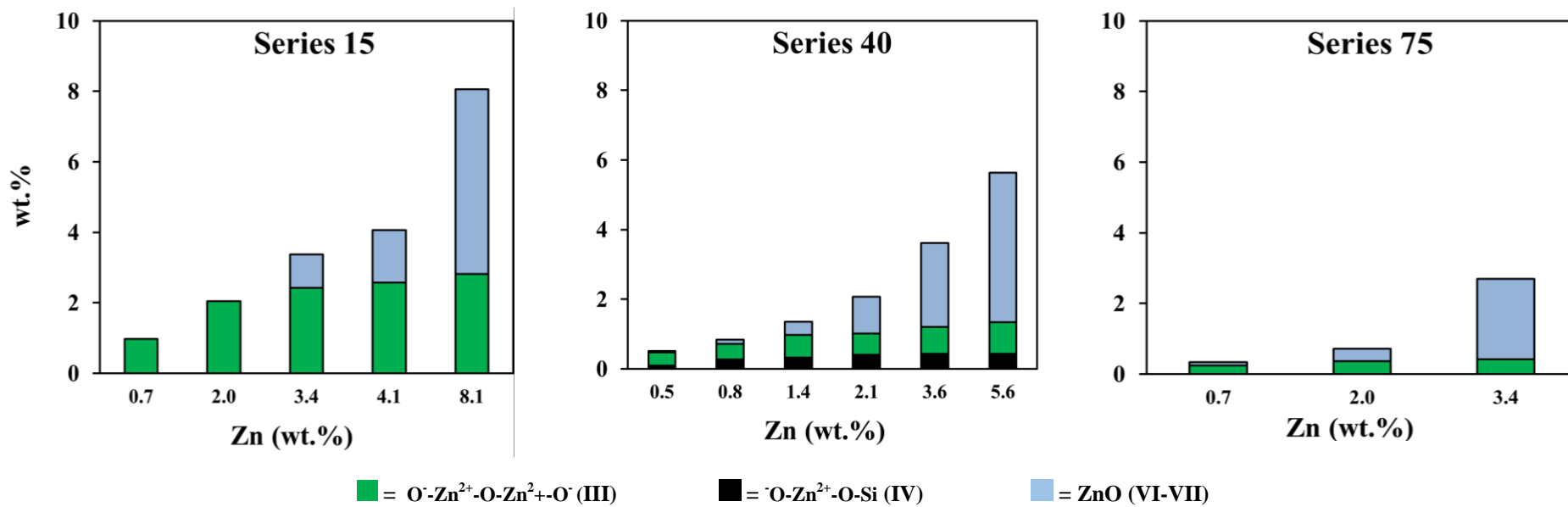


Figure 6: Bar chart of the molar distribution of the Zn species on series 15, 40 and 75.

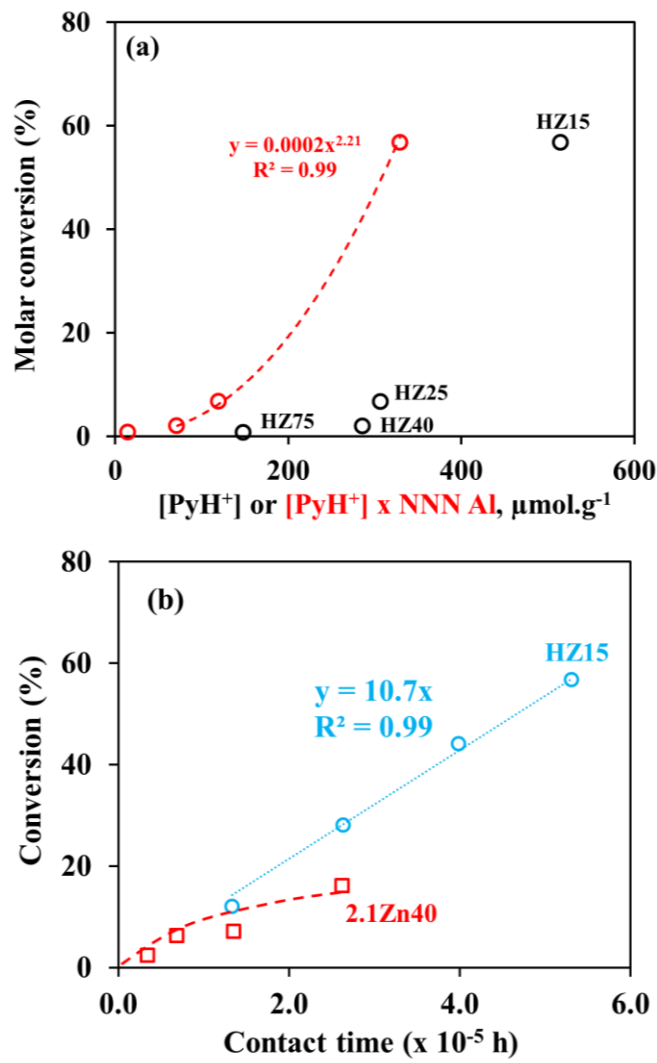
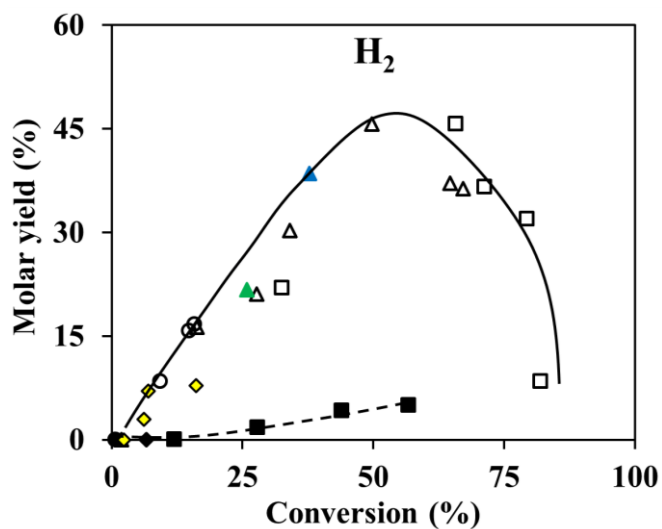
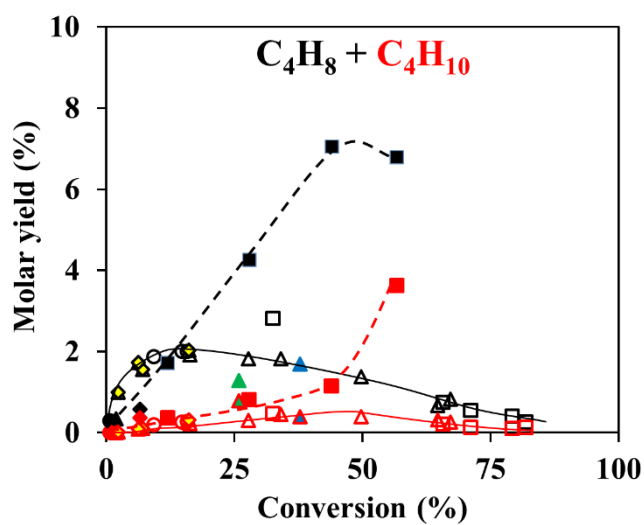
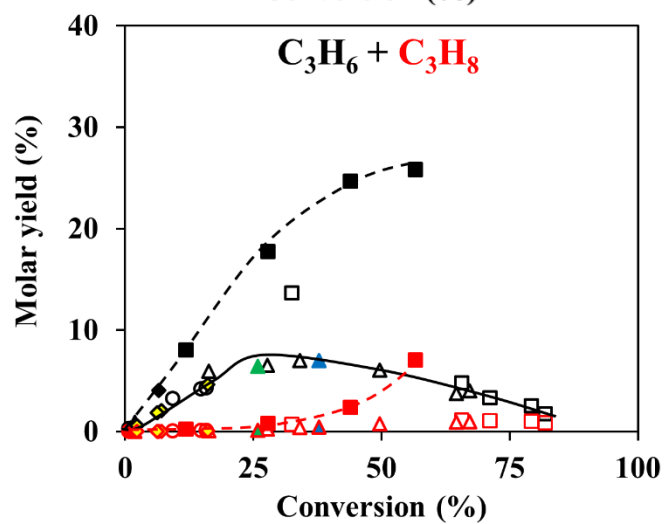
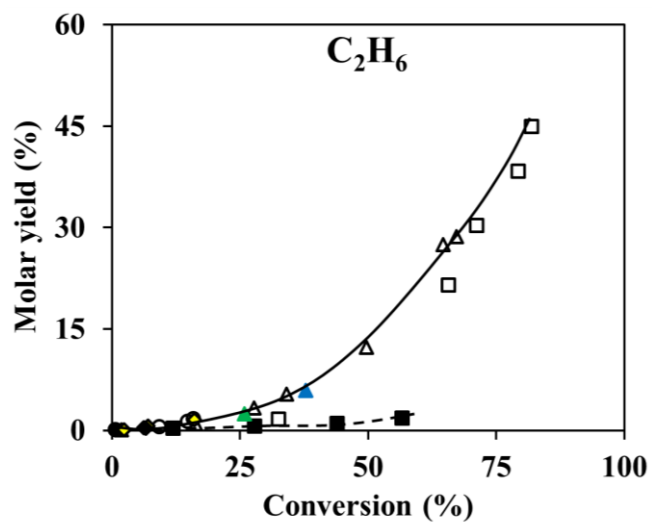
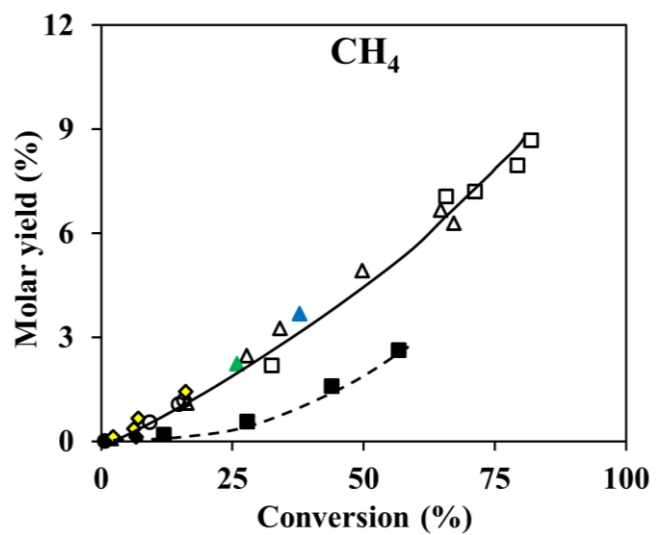


Figure 7: Light olefins conversion on protonic zeolites:
 (a) Ethylene conversion as a function of concentration of BAS (black symbol) and pair of BAS (red symbol).
 (b) Ethylene conversion as a function of contact time on HZ15 (blue symbol) and 2.1Zn40 (red symbol).





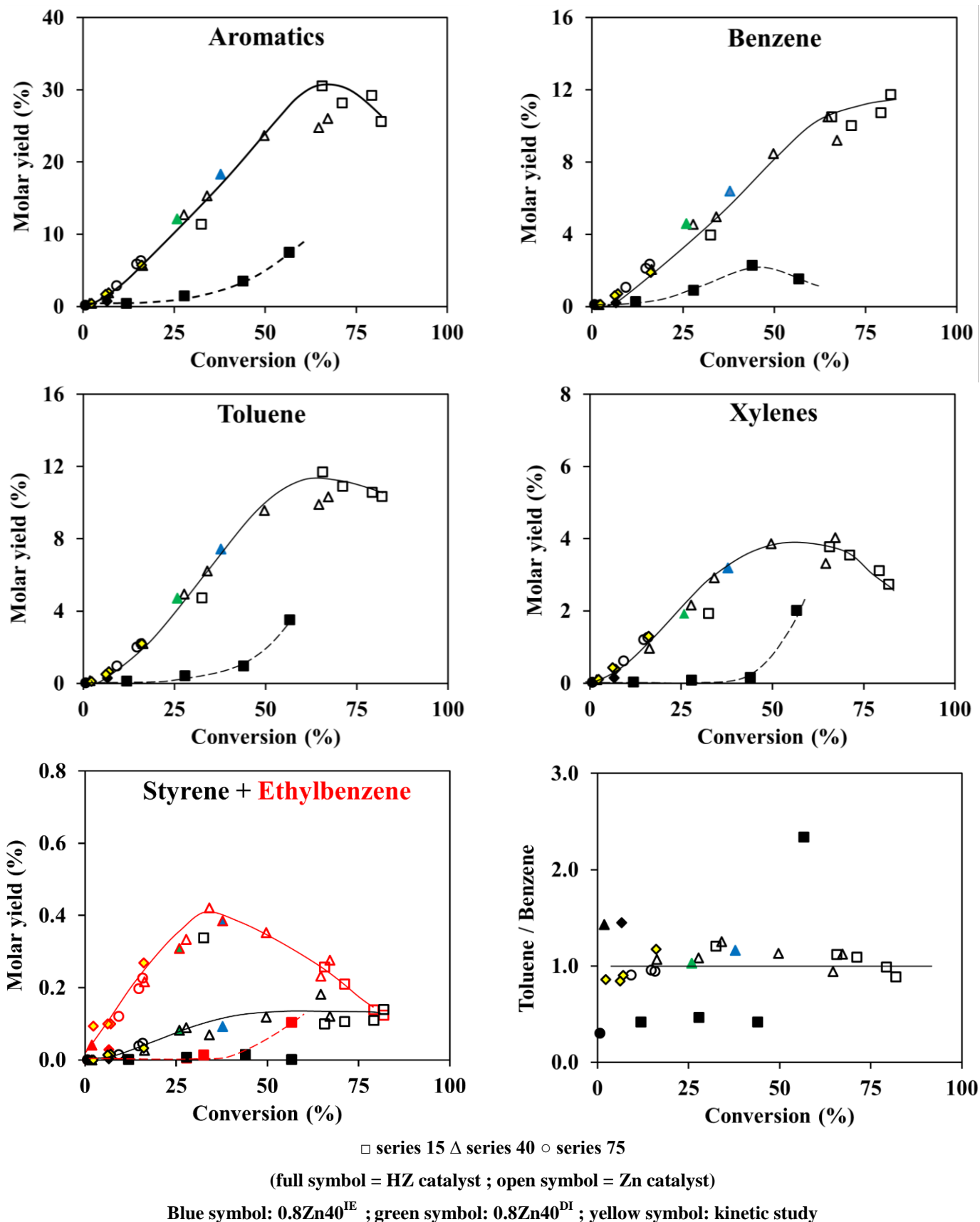


Figure 8: Molar yields of H₂, CH₄, paraffins: C₂-C₄ olefins: O₃-O₄ and aromatics: BTX, EB and styrene as a function of the conversion.

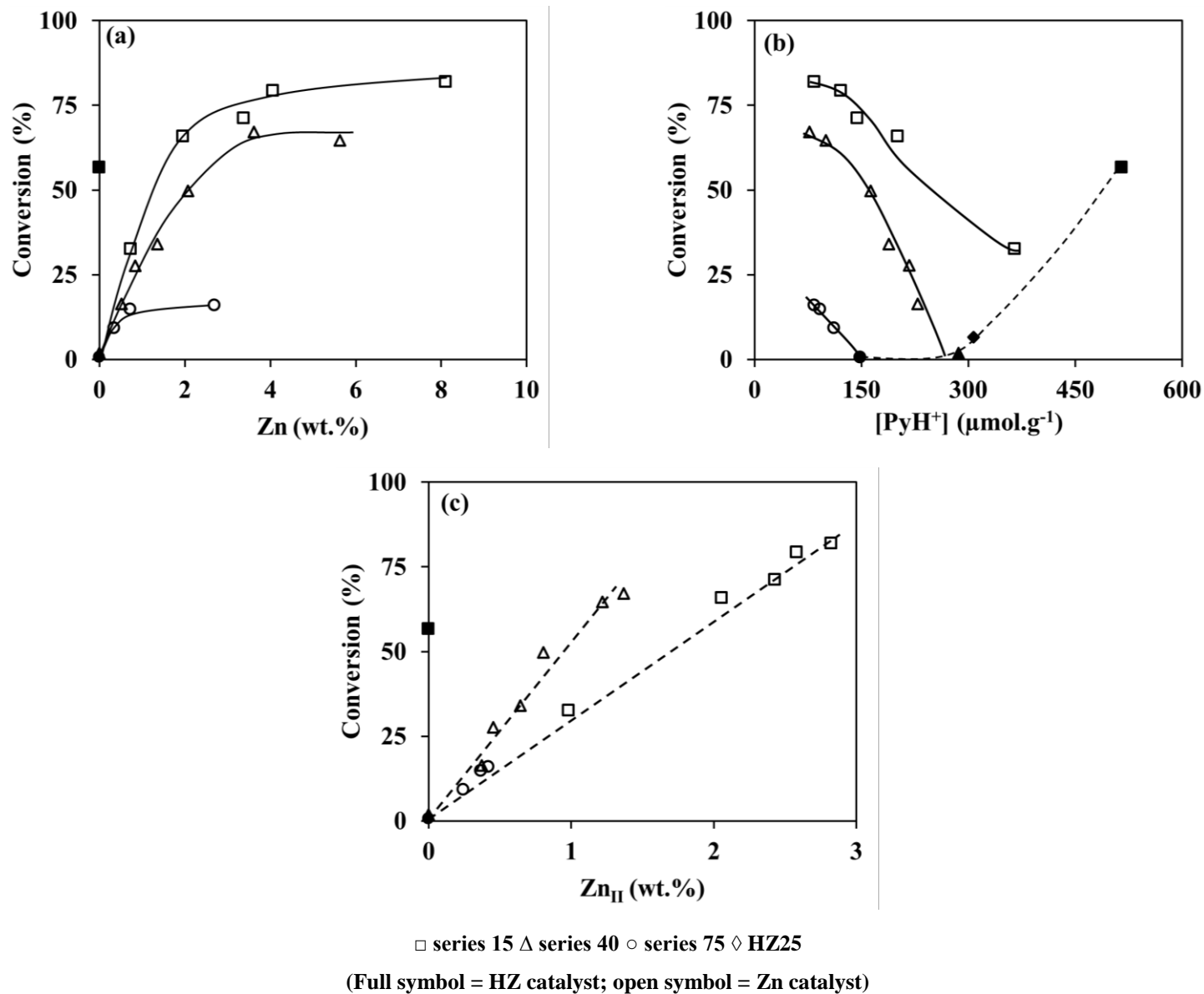
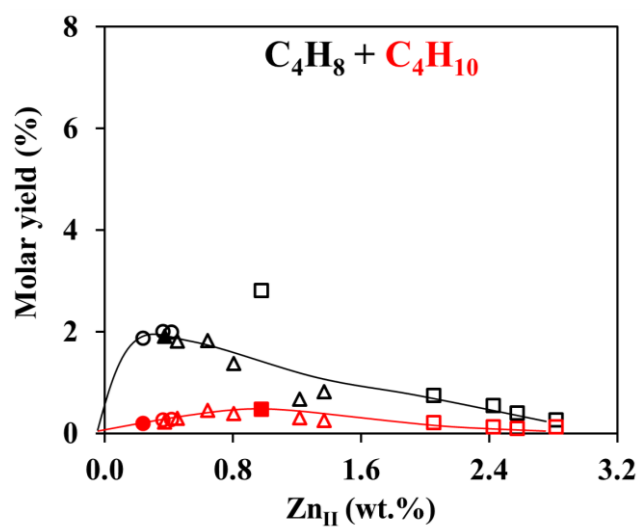
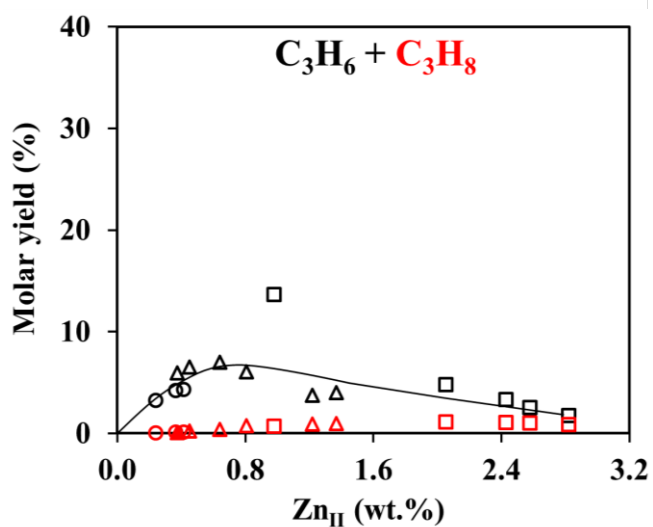
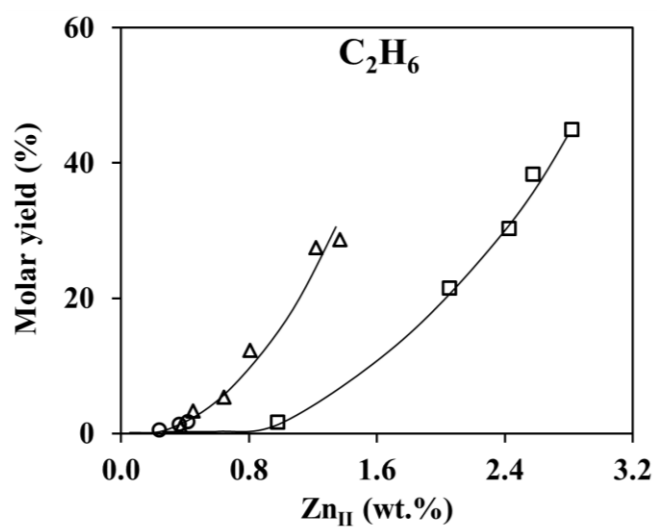
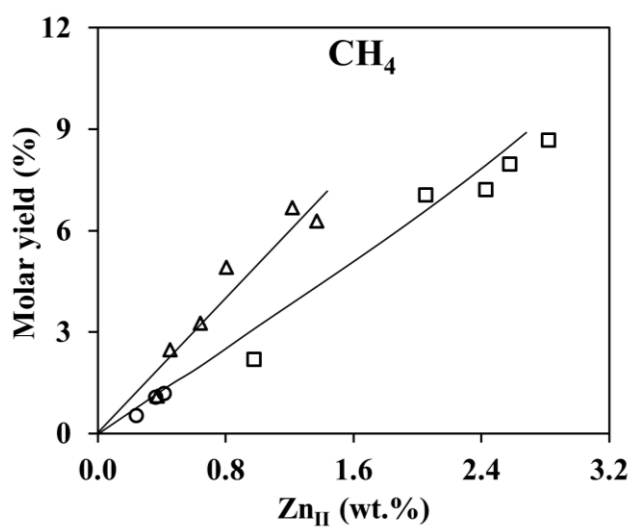
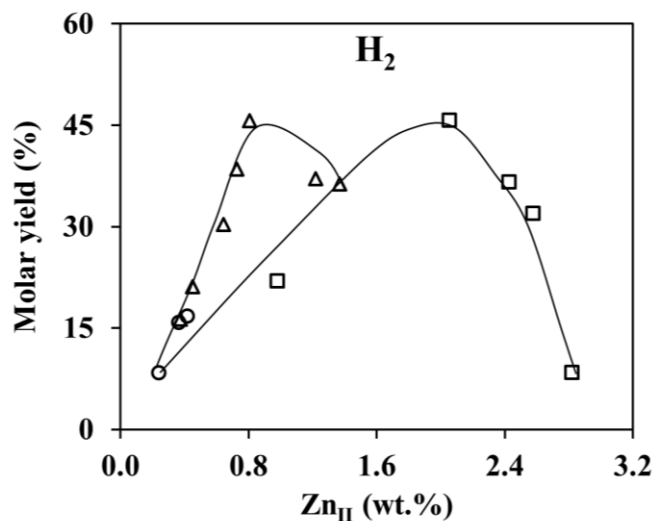


Figure 9: Ethylene conversion as a function of impregnated zinc content (a), concentration of Brønsted acid sites (b) and content of oxo-binuclear Zn cation.

(Operating condition: 500 °C, P= 1 atm, τ = 0.27 s)



□ series 15 △ series 40 ○ series 75

(full symbol = HZ catalyst ; open symbol = Zn catalyst)

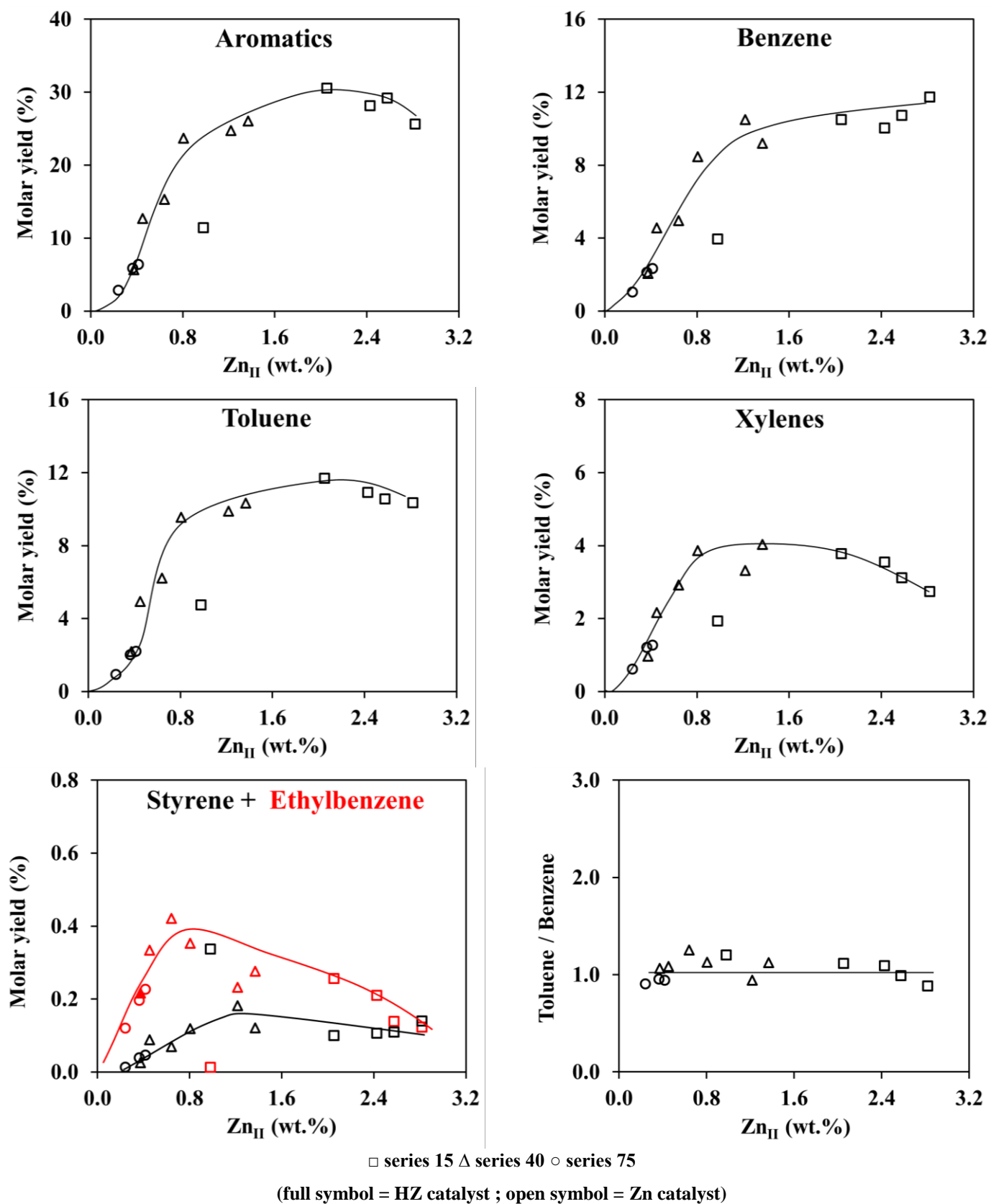


Figure 10: Molar yields of the products of ethylene transformation as a function of the content of oxobinuclear Zn cation.

